INTERNATIONAL CENTER FOR NUMERICAL METHODS IN ENGINEERING

On the Application of the Particle Finite Element Method (PFEM) to Problems in Civil Engineering

A. Larese de Tetto

Monograph CIMNE Nº-98, September 2006

On the Application of the Particle Finite Element Method (PFEM) to Problems in Civil Engineering

A. Larese de Tetto

Monograph CIMNE Nº-98, September 2006

International Center for Numerical Methods in Engineering
Gran Capitán s/n, 08034 Barcelona, Spain

INTERNACIONAL CENTER FOR NUMERICAL METHODS IN ENGINEERING
Edificio C1, Campus Norte UPC
Gran Capitán s/n
08034 Barcelona, sPAIN
www.cimne.upc.es

Fist edition: September 2006

ON THE APPLICATION OF PARTICLE FINITE ELEMENT METHOD (PFEM)
TO PROBLEM IN CIVIL ENGINEERING
Monograph CIMNE M98

ISBN: 84-96736-02-4

Depósito legal: B-46523-2006

Contents

Prefazione

Dopo la sua prima apparizione sul finire degli anni 50, il Metodo agli Elementi Finiti si è subito imposto come uno dei metodi numerici più potenti nonchè di relativamente semplice gestione, riuscendo a modellare facilmente geometrie anche notevolmente complesse ed essendo versatile e flessibile.

Le approssimazioni standard alla base del FEM si basano sul metodo di Galerkin o dei residui pesati, strumento potente ed efficace nel caso di problemi solido-strutturali portando ad ottenere matrici di rigidezza simmetriche, ma non altrettanto nell'approccio con problemi di fluido dinamica. Nella formulazione di fenomeni di flusso, infatti, la difficoltà più grande è dovuta alla presenza di un termine convettivo: gli operatori convettivi sono per loro stessa natura non simmetrici portando quindi alla perdita del più grande vantaggio della formulazione tradizionale.

Dopo aver brevemente riportato il percorso matematico che conduce alla definizione delle equazioni di Navier Stokes per la descrizione del comportamento dei fluidi definiti newtoniani, è stata affrontata la formulazione del metodo dei residui pesati. Da un lato viene toccato il problema della scelta degli spazi di velocità e pressione e dell'ordine delle funzioni interpolanti per queste variabili: la scelta infatti non può essere arbitraria se non si vuole compromettere seriamente la stabilità del problema. Dall'altro, invece, si pone particolare attenzione al fatto che il sistema finale del problema risulta non simmetrico e non lineare: la trattazione numerica può portare a serie oscillazioni della soluzione che possono allontanare quest' ultima dai valori reali, viene riportato un breve accenno alle tecniche di stabilizzazione per superare questa difficoltà.

Una volta trattato l'aspetto puramente numerico, viene presentato il

Particle Finite Element Method (PFEM), metodo di possibile utilizzo in molteplici campi anche se è nella risoluzione dei problemi di fluidi a superficie libera, onde d'urto e separazione di domini liquidi che trova la sua migliore applicazione.

Se il FEM tradizionale presenta i problemi tipici legati alla costruzione di una mesh che dev'essere conforme, deve avere elementi con forma quanto più regolare possibile e deve avere una frontiera ben definita; dall'altro lato, i meshless methods, sviluppati negli ultimi decenni, hanno sicuramente il vantaggio di aver bisogno esclusivamente del legame di connessione tra i nodi e di dare una soluzione che dipende esclusivamente dalla posizione di questi ultimi, ma presentano alcune difficoltà nel momento in cui la distanza tra i nodi sia variabile in una direzione preferenziale o abbia valori fortemente dissimili in zone diverse del dominio.

Dal tentativo di trasformare il FEM in un meshless method per guadagnare i vantaggi di entrambi gli approcci nasce quindi, quello che è stato definito *Meshless Finite Element Method* (MFEM): passo essenziale per raggiungere lo scopo è l'introduzione dell'*Extendended Delaunay tessellation* per la definizione delle funzioni di forma come viene ampiamente spiegato. Il PFEM usa il MFEM per computare le forze che agiscono su ogni particella: non si parla infatti di nodi, derivando questo approccio dai *particle methods* in cui tutte le informazioni, sia geometriche che meccaniche sono attaccate alla particella che può o meno corrispondere con un nodo nel caso di una mesh o con un punto nel caso di un meshless method. Ogni particella si muove concordemente alla sua massa (e quindi alla gravità) e alle forze dovute all'interazione con le particelle vicine.

La parte centrale del presente lavoro rappresentata dall'opera di validazione del programma *PFLOW* creato al CIMNE (Centro Internazionale di Metodi Numerici per l'Ingegneria di Barcellona) dall'Ing. Miguel Angel Celigueta e altri, tale programma utilizza chiaramente il PFEM. A tale scopo verranno presi dei dati sperimentali ricavati in analisi di laboratorio per diversi fenomeni e una volta ricostruite, con il supporto del GiD [1], le opportune geometrie, e assegnate le condizioni iniziali e al contorno legate all'esperimento reale, si opererà un raffronto tra i risultati numerici e quelli sperimentali.

Il primo esempio ricostruisce un modello creato per l'analisi della traiettoria e della pressione nel caso di un 'flip-bucket',struttura che si colloca generalmente alla base di uno sfioratore in uscita da una diga in modo da riuscire ad allontanare l'acqua dal piede della stessa, per non danneggiarlo. La verifica, nel primo caso, si focalizza sulla correttezza della traiettoria di un getto d'acqua e sui valori di pressione esercitati sulla struttura. Per comprendere quali siano i parametri che maggiormente influenzano la bontà dei risultati, più modelli verranno costruiti variando la dimensione della mesh o la velocità del flusso in entrata.

Un modello 3D verificherà infine che, con l'inserimento di un deflettore di deviazione del flusso, la traiettoria dell'onda che si viene a formare rispetti i dati misurati in laboratorio.

Dopo aver analizzato la traiettoria di un getto d'acqua, viene verificata la bontà del metodo in caso di efflusso sotto battente per la presenza di una paratoia piana: la contrazione del getto, la portata uscente, la pressione sulla paratoia saranno i parametri comparati. Verrà infine causata la formazione di un risalto idraulico ponendo una soglia alta sul fondo in modo da creare una corrente lenta di valle in contrasto con quella rapida in uscita dalla paratoia.

L'ultimo esempio vuole invece ricostruire il modello creato per l'analisi di pressioni e velocità nel caso di uno sfioratore a gradoni la cui costruzione, di origini antichissime ma poi abbandonata per questioni economiche, è ritornata ad essere molto popolare nel momento in cui è stato introdotto nel mercato il calcestruzzo compattato a rullo (CCR).

Chapter 1

Finite Elements in fluid dynamics

1.1 Abstract

Current chapter tries to give an overview of theoretic background necessary to deal with fluid dynamic problems with Finite Element Method (FEM) approach. Starting from a brief summary of the principle steps of the development of the theory, we analyze the differences between the classical world of solid structures and the world of fluids, finding out finally the principle equations that control these problems.

1.2 Introduction

From its first appearance in late 50's, due to M.J.Turner [2], the Finite Element Method (FEM) became one of the most powerful numerical method and it was used in a lot of different fields. The ease of modeling complex geometry was the main advantage of such a method, together with the possibility to use differential-type boundary conditions and to be programmed in a flexible way.

The Galerkin formulation of the method of weighted residuals, which is the approximation at the base of FEM, is really successful in case of structural or heat conduction problems, that is, in general, in problems governed by self adjoint partial differential equations, because of the symmetry of the stiffness matrix [3]. This optimality is lost in case of fluid dynamic problems and this is the reason of the later development of the use of FEM in this field. In fact, although the equations governing fluid flow and solid mechanics appear to be similar, a big difference occurs: even when fluid is in a steady state, convective acceleration appears. These convection operators are, for their own nature, non-symmetric and this mean that the ease of Galerkin formulation is lost when convection dominates the transport process.

A second problem arises with the numerical solution of incompressible flow problems and manifests itself when an inappropriate combination of elements interpolation function is employed: the consequence is an instability in pressure value also for slow flows, independently from Reynolds number [4]. In practice, solutions to convection-dominated transport problems by Galerkin method are often corrupted by serious node to node oscillations. These aspects led the development of different stabilization techniques, as we will see in this chapter, which permitted to overcome these problems and to have a strong impetus for the utilization of FEM in the simulation of fluid dynamics.

1.3 The governing equation of fluid dynamics

Before presenting Navier-Stokes problem it useful to point out the three equations that are at the base of the mathematical formulation. From one side we have the conservations equations that for the incompressible case are the same of the solid case, on the other side there is the constitutive low which underlines the biggest difference between solid and fluid: the inability of this last one to sustain shear stresses when at rest.

1.3.1 Conservation Equations

In the case of incompressible fluid two equations are sufficient to determine the problem, these are the Conservation of Mass and the Conservation of Momentum.

- ***Mass Conservation***: Considering any given domain Ω the mass that it contains can be expressed as:

$$m(\Omega) = \int_{\Omega} \rho(\mathbf{X}, t) d\Omega(t); \tag{1.1}$$

where $\rho(X,t)$ is the density of the considered material at point X.

During any time interval δt, the principle of conservation of mass implies that for any control volume the mass flow entering minus the mass flow leaving equals the change of mass within the control volume [5]; that is to say:

$$\frac{Dm(\Omega(t))}{Dt} = \frac{D}{Dt}\int_{\Omega}\rho(\mathbf{X},t)d\Omega = 0; \tag{1.2}$$

Considering Raynolds transport theorem that, for a general function $f(x,t)$, says that:

$$\frac{D}{Dt}\int_{\Omega(t)}\mathbf{f}(\mathbf{x},t)d\Omega = \int_{\Omega(t)}\left(\frac{Df}{Dt} \ + \ \nabla \bullet \mathbf{vf}\right) \ d\Omega; \tag{1.3}$$

we can obtain

$$\int_{\Omega}\left(\frac{D\rho}{Dt} \ + \ \rho\nabla \bullet \mathbf{v}\right) \ d\Omega = 0. \tag{1.4}$$

Because the domain is totally an arbitrary one we can be sure that

$$\frac{D\rho}{Dt} + \rho\nabla \bullet \mathbf{v} = 0. \tag{1.5}$$

If we do not consider thermal variation, that in any case can be separately taken into account, density usually follows a state equation pressure dependent, in fact

$$d\rho = \frac{\rho}{K}dp \quad \Rightarrow \quad d\rho = \frac{1}{c^2}dp \quad \Rightarrow \quad \frac{D\rho}{Dt} = \frac{1}{c^2}\frac{Dp}{Dt};$$

being K the bulk modulus of elasticity and c the wave propagation velocity.

The behavior of the fluid we are going to analyze can be consider, as for many other fluids, incompressible, that is to say that pressure is constant in time and, therefore density is not time dependent; equation 1.5 reduces to:

$$\nabla \bullet \mathbf{v} = 0; \tag{1.6}$$

that is the basic equation for treatment of incompressible flows.

- ***Conservation of Linear Momentum***: it is nothing else but the second law of motion known as Second Newton's Law and it connects all forces, both superficial (acting on the surface Γ) and volumetric one (acting on the volume Ω), with the acceleration of the body. Given a domain Ω of boundary Γ, calling the body forces acting on this domain b, and boundary tractions t, we can write that:

$$\mathbf{f}(\Omega, t) = \int_{\Omega} \rho b(\mathbf{x}, t) d\Omega \ + \ \int_{\Gamma} t(\mathbf{x}, t) d\Gamma. \tag{1.7}$$

Linear momentum is for definition:

$$\mathbf{p}_{lin}(\Omega, t) = \int_{\Omega} \rho(\mathbf{x}, t)\mathbf{v} d\Omega. \tag{1.8}$$

Therefore the second Newton's law is

$$\frac{D\mathbf{p}_{lin}(\Omega, t)}{Dt} = \mathbf{f}(t); \tag{1.9}$$

that is to say, considering the Reynolds transport theorem,

$$\frac{D\mathbf{p}_{lin}(\Omega, t)}{Dt} = \int_{\Omega} \frac{D\rho\mathbf{v}}{Dt} + \rho\mathbf{v}\nabla\bullet\mathbf{v} d\Omega = \int_{\Omega} \rho\frac{D\mathbf{v}}{Dt} + \mathbf{v}\left(\frac{D\rho}{Dt} \ + \ \rho\nabla\bullet\mathbf{v}\right) d\Omega. \tag{1.10}$$

This expression can become much more simple considering the equation of mass conservation that simplifies some terms

$$\frac{D\mathbf{p}_{lin}(\Omega, t)}{Dt} = \int_{\Omega} \rho\frac{\partial\mathbf{v}}{\partial t} d\Omega; \tag{1.11}$$

and using the divergence theorem that permits to pass from an integral of surface to a linear one

$$\int_{\Gamma} \mathbf{t} d\Gamma = \int_{\Gamma} \mathbf{n}\bullet\sigma d\Gamma \ = \ \int_{\Omega} \nabla\bullet\sigma \ d\Omega. \tag{1.12}$$

Therefore after some mathematical passages we obtain:

$$\rho\frac{D\mathbf{v}}{Dt} = \nabla\bullet\sigma \ + \rho \ \mathbf{b}; \tag{1.13}$$

which is the strong form of the equation of momentum conservation.

1.3.2 Constitutive Relation

As we take into account strain and rotation in the case of a solid, we have to take into account rate of strain and rate of rotation in the case of a fluid: the analysis of the relative motion of neighboring particles within a fluid is similar to the theory of deformation of an elastic body. An important variable is for sure the *velocity gradient*, that, in a Cartesian coordinate system, is:

$$\nabla\mathbf{v} = \begin{pmatrix} \frac{\partial v_1}{\partial x_1} & \frac{\partial v_1}{\partial x_2} & \frac{\partial v_1}{\partial x_3} \\ \frac{\partial v_2}{\partial x_1} & \frac{\partial v_2}{\partial x_2} & \frac{\partial v_2}{\partial x_3} \\ \frac{\partial v_3}{\partial x_1} & \frac{\partial v_3}{\partial x_2} & \frac{\partial v_3}{\partial x_3} \end{pmatrix}; \tag{1.14}$$

and can be decomposed in a symmetric and in a skew-symmetric part

$$\frac{\partial v_i}{\partial x_j} = \frac{1}{2}\left(\frac{\partial v_i}{\partial x_j} + \frac{\partial v_j}{\partial x_i}\right) + \frac{1}{2}\left(\frac{\partial v_i}{\partial x_j} - \frac{\partial v_j}{\partial x_i}\right); \tag{1.15}$$

for $i, j = 1, \ldots, n_{sd}$, otherwise written as

$$\nabla\mathbf{v} = \nabla^{\mathbf{s}}\mathbf{v} + \nabla^{\mathbf{w}}\mathbf{v}, \qquad \text{where} \quad \begin{cases} \nabla^{\mathbf{s}} := \frac{1}{2}(\nabla + \nabla^{\mathbf{T}}) \\ \nabla^{\mathbf{w}} := \frac{1}{2}(\nabla - \nabla^{\mathbf{T}}) \end{cases} \tag{1.16}$$

The symmetric tensor $\nabla^{\mathbf{s}}\mathbf{v}$ in called *rate of deformation tensor*, whereas the skew-symmetric one $\nabla^{\mathbf{w}}\mathbf{v}$ is the *vorticy tensor*.

Solid and flow problems are similar under many points of view but there is a big difference: in fact fluids are not able to support shear stresses if at rest, only pressure or a mean compressive stress can be carried, that is to say that the stress tensor, for a fluid at rest, has the isotropic form

$$\sigma_{ij} = -p\delta_{ij}, \tag{1.17}$$

where p is the static fluid pressure and δ_{ij} is the Kronecker delta. If the fluid is in motion the situation is different because of the presence of a non-zero term for tangential stresses and because the normal part of the stress depends on the direction of the normal to the element. In the case of incompressible or nearly-incompressible fluid it is convenient to separate thew isocoric and the deviatoric part of the stress tensor, that is:
isocoric term:

$$p := \frac{1}{3}Tr(\sigma) = \frac{1}{3}\sigma_{ij}; \tag{1.18}$$

deviatoric term:

$$\tau \ := \sigma \ - \ p\mathbf{I} \quad \rightarrow \quad \tau_{ij} \ := \ \sigma_{ij} - \delta_{ij}\frac{1}{3}\sigma_{ij}. \tag{1.19}$$

In the case of *Newtonian fluid* it is usually assumed that stress tensor and strain rate tensor are linearly related [3].
Being the strain rate tensor

$$\dot{\epsilon_{ij}} \ := \ \frac{1}{2}\left(\frac{\partial v_i}{\partial x_j} \ + \ \frac{\partial v_j}{\partial x_i}\right); \tag{1.20}$$

the constitutive relation can be assumed to be in the form

$$\tau \ = \ 2\mu\left(\dot{\epsilon} - \frac{1}{3}Tr(\dot{\epsilon})\mathbf{I}\right) \rightarrow \tau \ = \ 2\mu\left(\dot{\epsilon_{ij}} - \frac{1}{3}\dot{\epsilon_{ij}}\right); \tag{1.21}$$

where μ is the dynamic viscosity.

Therefore the Cauchy stress, using the 1.21, is

$$\sigma \ = \ \tau \ + \ p\mathbf{I} \ = \ 2\mu\left(\dot{\epsilon} \ - \ \frac{1}{3}Tr(\dot{\epsilon})\mathbf{I}\right) \ + \ p_0\mathbf{I}; \tag{1.22}$$

that written in function of the velocity is

$$\sigma_{ij} \ = \ \mu\left(\frac{\partial v_i}{\partial x_j} \ + \ \frac{\partial v_j}{\partial x_i}\right) \ - \ \frac{2}{3}\mu\frac{\partial v_k}{\partial x_k}\delta_{ij} \ + \ p\delta_{ij}; \tag{1.23}$$

and reducing the analysis at the case of incompressible fluid ($\nabla \ \bullet \ \mathbf{v} = 0$)

$$\sigma_{ij} \ = \ \mu\left(\frac{\partial v_i}{\partial x_j} \ + \ \frac{\partial v_j}{\partial x_i}\right) \ + \ p\delta_{ij}. \tag{1.24}$$

If we want the Stokes law in compact form:

$$\sigma \ = \ -p\mathbf{I} \ + \ 2\mu\nabla^s\mathbf{v}; \tag{1.25}$$

1.4 The Navier-Stokes equations

The Navier-Stokes equations are always used to describe the dynamic effect of a newtonian fluid subjected to external forces, and the relation between these forces and the internal one. We can in general obtain these equations putting the conservations lows 1.5 and 1.13 into the constitutive relation 1.23

but, considering that the statement of incompressible fluid is something commonly accepted for civil engineering applications, we can put the 1.6 and 1.13 into 1.25 [6].

$$\rho\frac{Dv}{Dt} = \nabla \bullet \sigma + \rho\mathbf{b} = \nabla \bullet 2\mu\nabla^s v + \nabla \bullet \mathbf{pI} + \rho\mathbf{b}; \tag{1.26}$$

Considering the development of the time derivative of the velocity:

$$\frac{Dv}{Dt} = \frac{\partial v}{\partial t} + (\mathbf{v} \bullet \nabla)\mathbf{v};$$

and introducing the kinematic viscosity $\nu = \frac{\mu}{\rho}$ becomes

$$\frac{\partial v}{\partial t} + (\mathbf{v} \bullet \nabla)\mathbf{v} - 2\mu\nabla \bullet \nabla^s\mathbf{v} + \nabla \bullet \mathbf{pI} + \mathbf{b} = 0; \tag{1.27}$$

Knowing that $\nabla \bullet \mathbf{pI} = \nabla\mathbf{p}$ and introducing the definition of the $\nabla^s\mathbf{v}$, we can obtain

$$2\nu\nabla \bullet \nabla^s\mathbf{v} = \nu\nabla \bullet \nabla\mathbf{v} + \nu\nabla \bullet \nabla\mathbf{v}^T = \nu\nabla^2\mathbf{v} + \nu\nabla(\nabla \bullet \mathbf{v}); \tag{1.28}$$

so that

$$\frac{\partial v}{\partial t} + (\mathbf{v} \bullet \nabla)\mathbf{v} - \nu\nabla(\nabla \bullet \mathbf{v}) + \nabla\mathbf{p} = \mathbf{b}; \tag{1.29}$$

Inserting, as said before, the condition over the mass conservation 1.6 of incompressible fluid:

$$\frac{\partial v}{\partial t} + (\mathbf{v} \bullet \nabla)\mathbf{v} + \nabla\mathbf{p} = \mathbf{b}; \tag{1.30}$$

$$\nabla \bullet \mathbf{v} = 0; \tag{1.31}$$

this is the typical form of the Navier-Stokes equations used to discretized the problem.

1.4.1 Galerkin formulation for stationary flow

Following Galerkin approach to the Navier-Stokes problem, we have to introduce an approximation on both velocity and pressure components, as well as for their associating weighting residuals, that leads to a *mixed finite elements method* [3]. The success of such a method is due to the fact that velocity and pressure are locally interpolated and pressure gradient is not present in the weak form, that is, it is not necessary that pressure is continuous at the interface between elements.

Looking at the role that pressure has in such a problem , we can see that it can not be represented by a constitutive low because it is only a lagrange multiplier with the precise aim to “correct” itself to allow velocity to respect the incompressibility constraint, that is the divergence free condition. This usually carries to badly conditioned problems, being these latter often expressed in function of $(\mathbf{v}, p)$ arriving also sometimes to get a singular matrix [3]; to avoid this problem it is useful to start the analysis of the *Stationary Stokes problem.* Taking into account this simplification we can forget the convective and the time dependent terms; the equations become:

$$-\nu\nabla^2\mathbf{v} \ + \ \nabla\mathbf{p} \ = \ \mathbf{b} \tag{1.32}$$

$$\nabla \bullet \mathbf{v} \ = \ 0 \tag{1.33}$$

and applying Galerkin discretization [3] we write the problem in matrix form as follow

$$\begin{pmatrix} \mathbf{K} & \mathbf{G} \\ \mathbf{G^T} & \mathbf{0} \end{pmatrix} \cdot \begin{pmatrix} \mathbf{u} \\ \mathbf{p} \end{pmatrix} = \begin{pmatrix} \mathbf{f} \\ \mathbf{h} \end{pmatrix}; \tag{1.34}$$

the meaning of each term of the system can be easily understood:

- $-\nu\nabla^2\mathbf{v} \quad \rightarrow \quad \mathbf{Kv}$
- $\nabla\mathbf{p} \quad \rightarrow \quad \mathbf{Gp}$
- $\nabla \bullet \mathbf{v} \quad \rightarrow \quad \mathbf{G^T p}$

where **K** is the *viscosity matrix* obtained from the assembly of the contribution of each element; **G** is the discrete *gradient operator* and $\mathbf{G^T}$ is the discrete *divergence operator*, whereas **f** and **h** are forces and reactions incorporating the Neumann and Dirichlet boundary conditions. The problem that arose is connected with the understanding of the necessity to make the system solvable in fact a null submatrix appear on the diagonal of 1.34 and it can makes more difficult to ensure a non-zero determinant: as largely explained in [3], it can be demonstrated that providing the *kernel* of matrix **G** is zero, then **u** and **p** are uniquely described being the matrix of 1.34

non-singular. For definition

$$ker\mathbf{G} \;:=\; \{\mathbf{q} \mid \mathbf{Gq} \;=\; \mathbf{0}\}\,.$$

To confirm this equation, velocity and pressure interpolation must satisfy the Ladyzhenskaya (1969), Babuska (1970/71) and Brezzi (1974) condition (LBB condition) which is necessary to guarantee the stability of a mixed method. This condition, otherwise known as *inf-sup* condition, underlines that velocity and pressure spaces cannot be chosen arbitrarily but there must be a clear connection between them, if this is respected, then the discrete gradient operator $\mathbf{G}$ is such that $ker\mathbf{G} \;=\; 0$, the pressure matrix $(\mathbf{G^T K^{-1} G})$ is positive definite and the partitioned matrix 1.34 is non-singular. It means that families of elements characterized by different orders interpolation have to exists for velocity and pressure, and we can find many in literature. Modern approach tends to focus its attention on the *equal-order interpolations*: what they want to do is, looking at the 1.34, to make the zero term, resulting from the imposition of the incompressibility condition, become a non-zero one. Some examples of these techniques can be the Galerkin Least Squares (GLS) or the Finite Elements calculus (FIC) for examples [3].

1.4.2 Galerkin formulation for steady flow

Taking away the condition of stationary state, the biggest difference is the comparison of a convective term in the partitioned matrix 1.34 :$\mathbf{C}(\mathbf{v})$ deriving from the discretization of $(\mathbf{v} \cdot \nabla)\mathbf{v}$ (1.31); 1.34 becomes:

$$\begin{pmatrix} \mathbf{K} + \mathbf{C}(\mathbf{v}) & \mathbf{G} \\ \mathbf{G^T} & \mathbf{0} \end{pmatrix} \cdot \begin{pmatrix} \mathbf{u} \\ \mathbf{p} \end{pmatrix} = \begin{pmatrix} \mathbf{f}(\mathbf{v}) \\ \mathbf{h} \end{pmatrix}. \tag{1.35}$$

System 1.35 is non-symmetric and non-linear that is an appropriate iterative solution has to be used. Fortunately some stabilization techniques help the resolution also of this second problem due to the presence of a convective term: in case of high Reynolds number, that is when convection dominates on the viscosity effects, and in absence of any stabilization, the finite element calculus can tend to oscillatory solution that soon can be really far from the real phenomenon. The basic step to overcome the problem will be briefly analyzed in this paragraph, but for a large and detailed treatment of the subject the consultation of [4] is recommended.

The starting point in this case is given by the convection-diffusion problem, that is by the following equation:

$$(\mathbf{a} \bullet \nabla)\mathbf{v} - \nu\nabla^2\mathbf{v} = s; \tag{1.36}$$

where $\mathbf{a}$ is the convective velocity and $s = s(x)$ is a volumetric source term. If we want the weak form, then we obtain

$$\int_\Omega \omega(\mathbf{a} \bullet \nabla)\mathbf{v}\ d\Omega - \int_\Omega \nu\omega\nabla \bullet (\nabla\mathbf{v})\ d\Omega = \int_\Omega \omega s\ d\Omega; \tag{1.37}$$

where ω is a function test which is zero in the Dirichlet boundary.

Using the Green-Gauss theorem [1] the equation becomes:

$$\int_\Omega \omega(\mathbf{a} \bullet \nabla)\mathbf{v}\ d\Omega - \int_\Omega \nabla\omega \bullet \nu\nabla\mathbf{v}\ d\Omega = \int_\Omega \omega s\ d\Omega; \tag{1.39}$$

Considering the classical Galerkin approach, the discrete form of this problem take the form

$$(\mathbf{C} + \mathbf{K})\mathbf{v} = \mathbf{f} \tag{1.40}$$

where $\mathbf{C}$ and $\mathbf{K}$ are the matrices obtained by the assembling of the contribution of each element:

$$\mathbf{C}^e_{ab} = \int_{\Omega^e} N_a(a \bullet \nabla\mathbf{N_b})\ d\Omega \tag{1.41}$$

$$\mathbf{K}^e_{ab} = \int_{\Omega^e} \nu\nabla N_a \bullet (\nabla\mathbf{N_b})\ d\Omega \tag{1.42}$$

$$\mathbf{f}^e_a = \int_{\Omega^e} \omega N_a s\ d\Omega \tag{1.43}$$

As simple example we can treat the one dimensional case analytically considering a linear and regular element: the 1.37 becomes

$$a\frac{\partial v}{\partial x} - \nu\frac{\partial^2 v}{\partial x^2} = s \tag{1.44}$$

---

[1]

$$\int_\Omega \omega\nabla^2\mathbf{u}\ d\Omega = -\int_\Omega \nabla\omega \bullet \nabla\mathbf{u} - \nabla \bullet \omega\nabla\mathbf{u}\ d\Omega = \int_\Omega \nabla\omega \bullet \nabla\mathbf{u}\ d\Omega - \int_\Gamma \omega(\mathbf{n} \bullet \nabla\mathbf{u})\ d\Gamma; \tag{1.38}$$

and considering a constant size h and a constant source $s = 1$ the discrete operators become:

$$\mathbf{C^e} = \frac{a}{2}\begin{pmatrix} -1 & 1 \\ -1 & 1 \end{pmatrix}; \tag{1.45}$$

$$\mathbf{K^e} = \frac{\nu}{h}\begin{pmatrix} 1 & -1 \\ -1 & 1 \end{pmatrix}; \tag{1.46}$$

$$\mathbf{f^e} = \begin{pmatrix} \frac{1}{2} \\ \frac{1}{2} \end{pmatrix}; \tag{1.47}$$

assembling the different contributions we obtain:

$$a\frac{v_{j+1} - v_{j-1}}{2h} - \nu\frac{v_{j+1} - 2v_j + v_{j-1}}{h^2} = 1; \tag{1.48}$$

and introducing the *Peclet number* [4]

$$Pe = \frac{ah}{2\nu}$$

we can write

$$\frac{a}{2h}\left(\frac{Pe-1}{Pe}v_{j+1} + \frac{2}{Pe}v_j - \frac{Pe+1}{Pe}v_{j-1}\right) = 1. \tag{1.49}$$

This algebraic equation is non-symmetric and in addiction the accuracy deteriorates as the parameter Pe increases, arriving to an absurd for $Pe \rightarrow \infty$ this statement means that only convective terms are of importance and it brings to a purely oscillatory solution with no relation with the physical problem. Taking into account a length = 1 the analytic solution is

$$u(x) = \frac{1}{a}\left(x - \frac{1 - exp\ \gamma h}{exp\ \gamma h}\right) \quad ; \quad \gamma := \frac{a}{\nu} \tag{1.50}$$

from that one the equation that exactly reproduce the analytic solution can be deduced and can be written in the form

$$a\frac{v_{j+1} - v_{j-1}}{2h} - (\nu - \bar{\nu})\frac{v_{j+1} - 2v_j + v_{j-1}}{h^2} = 1 \tag{1.51}$$

with

$$\bar{\nu} := \left(coth\ Pe - \frac{1}{Pe}\right)\nu Pe; \tag{1.52}$$

If we compare the 1.48 with the 1.52 we can observe that Galerkin introduces a spurious negative numerical diffusion. That implies that the oscillatory problem shown by Galerkin space discretization can be effectively corrected introducing a numerical diffusion.

Chapter 2

Particle Finite Elements Method (PFEM)

2.1 Abstract

The current chapter tries to present the Particle Finite Element Method (PFEM): it is explained what it is, starting from its origin from meshless FEM, continuing underlining the problems that it has been conceived to overcome, and ending with the presentation of the solutions it proposes.

2.2 Introduction

After the big success of Finite Element Method (FEM) started in late 50's, the so called meshless methods have been developed in the last decade both for structural and fluid mechanics problems; these techniques were presented first by Nayroles and later developed to solve structural mechanics problems by Belytschko et al. or fluid mechanics problems by Oñate et al. These new methods use the idea of a polynomial interpolant that fits a number of points minimizing the distance between the interpolated function and the value of the unknown points.

Geometry of the domain changes with time in many physical problems and this means that two nodes that are close to each other in a time step can be really far from each other in the following step, distortions can be large and hence a continuous remeshing is necessary to update the node connectivities; this should be done without an excessive loss of time, in a quickly way, in a fixed and bounded number of operations.

The definition of the free surface in fluid mechanics phenomena can be a typical problem: the domain is an unknown and can break in many free surface or many free surface can be jointed in a single one.

That of particle methods is an other class of methods very interesting for fluid dynamics problems. They represent the development of a physical phenomenon by a collection of points named particles [7]. In this case each particle moves accordingly to its own mass and to the forces, both internal and external, applied to it. A particle can be a physical part of the domain, such as a rock or a specific part of the continuous domain, but it is not necessary that it coincides with the node in a mesh or with the points in a meshless method.

In a particle method all the physical and mathematical properties are attached to the particle itself and not to the elements as in the FEM.

Particle Finite Elements Method is a special class of particle methods that combines standard characteristics of class of method with a background mesh with special finite element shape functions as it will be presented in this chapter.

2.3 Meshless method

The idea of a meshless method became quite popular in the last years because mesh generation, overall in 3D case, is the most time consuming technique within computational mechanics. To consider a way that does not require the generation of the mesh can solve partially this problem. Meshless methods require node connectivity to define interpolations and the same node connectivity is what influences the accuracy most than everything else.

The definition of meshless method itself is rather complex. A meshless method is an algorithm that satisfies both of the following statements:

- The definition of the shape functions depends only on the nodes position.
- The evaluation of the nodes connectivity is bounded in time and it depends exclusively on the total number of nodes in the domain.

It is easy to see as the FEM is not of course a meshless method. In fact a same point distribution in FEM can have different shape functions and the evaluation of nodal connectivity does not have to be necessary bounded in time to give accurate results

Considering an arbitrary nodes distribution in space, the biggest difficulties in building a mesh are represented by three points:

- it must be *conforming*;
- the shape of the elements has to be as much *regular* as possible;
- *boundary contours* must be respected.

Meshless methods on the contrary, do not need a conforming mesh but only the connectivities between nodes in order to build the approximation functions. Major problems in this kind of techniques are obviously given by the absence of a mesh, such as to say by the need of a variable distance between nodes, named h. In the case h presents some problems, as the only one direction variability, it can become really difficult to find out the node connectivity, and in some case the computing time can be of the same order than the most difficult mesh generation problem; it is for that reason that we can say that a meshless method is useless without a bounded evaluation of the node connectivity.

Both meshless method and FEM present problems with boundary contour.

2.4 The Meshless Finite Element Method (MFEM)

Having FEM advantages where meshless method has difficulties and *vice versa*, it seems a good idea to find out if it is possible to transform FEM in order to obtain a meshless method.

To better understand the following steps it is better to point out some classical definitions: given a set of distinct nodes $\mathbf{N} = \{\mathbf{n_1}, \mathbf{n_3}, \mathbf{n_3}, ..., \mathbf{n_n}\}$ [8]

- *The Voronoï diagram* of the set $\mathbf{N}$ is a partition of R^3 into region V_i (closed and convex or unbounded), where each region V_i is associated with a node $\mathbf{n_i}$, such that any point in V_i is closer to $\mathbf{n_i}$ than to any other node $\mathbf{n_i}$. The Voronoï diagram is unique.

Figure 2.1 Voronoï diagram, Voronoï circle and Delaunay triangulation for a 4 nodes distribution in 2D.

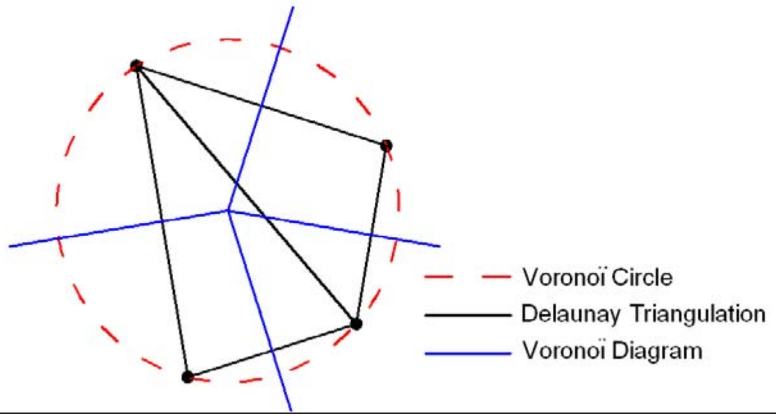

- *A Voronoï sphere* within the set **N** is any sphere, defined by 4 or more nodes, that contains no other node inside. Such sphere are otherwise known as empty circumspheres.

- *A Delaunay tessellation* within the set **N** is a partition of the convex hull Ω of all the nodes into region Ω_i such that $\Omega = \bigcup \Omega_i$ where each Ω_i is the tetrahedron defined by 4 nodes of the same Voronoï sphere.

Delaunay tessellations of a set **N** are not unique, on the other hand, the Voronoï diagram is unique thus it seems more reasonable to define meshless shape functions based on the unique Voronoï diagram than on the Delaunay tessellations. Furthermore in 3D problems the Delaunay tessellation may generate several tetrahedra of zero or almost zero volume (*slivers* [8]) which introduce many inaccuracies into the shape function derivatives; this is the reason why the Delaunay tessellation has to be improved iteratively violating the second statement that define a meshless method, being time unbounded in this case.

A new tessellation is now introduced to overcome these two problems:

- *The Extended Delaunay tessellation* within the set **N** is the unique partition of the convex hull Ω of all the nodes into regions Ω_i such that $\Omega = \bigcup \Omega_i$ where each Ω_i is the polyhedron defined by all the nodes laying on the same Voronoï sphere.

In this case the big difference is due to the fact that the nodes belonging to the same Voronoï sphere define a unique polyhedron. The only problem can be that only four nodes are necessary to define a sphere and it is possible that nodes very close to each other define spheres nearly coincident. To avoid this situation a parameter δ is introduced: the polyhedron is defined by all the nodes of the same Voronoï sphere and nearby sphere with a distance between center points smaller than δ. Considering two Voronoï spheres with nearby centers $\mathbf{c_i}$, because they are empty, they must satisfy the following steatment:

$$\mid r_2 - r_1 \mid \leq \mid\mid \mathbf{c_1} - \mathbf{c_2} \mid\mid; \tag{2.1}$$

being r the radii and $\mathbf{c}$ the centers.

Hence two spheres are similar if they satisfy:

$$\mid\mid \mathbf{c_1} - \mathbf{c_2} \mid\mid \leq \delta r_{rms}; \tag{2.2}$$

where δ is a small non dimensional value and r_{rms} is the root-mean-square radius. Two polyhedra will be joint if they belong to similar spheres.

Once the domain partition is defined, shape functions must be introduced: in order to define them inside each polyhedron, the non-Sibsonian interpolation will be used [4]. Considering the set of nodes belonging to a polyhedron: $\mathbf{P} = \mathbf{n_1}, \mathbf{n_2}, ..., \mathbf{n_m}$, the shape function $N_i(\mathbf{x})$ corresponding to the node $\mathbf{n_i}$ at an internal point $\mathbf{x}$ is defined by computing

$$N_i(\mathbf{x}) = \frac{\frac{s_i(\mathbf{x})}{h_i(\mathbf{x})}}{\sum_{j=1}^{m} \frac{s_j(\mathbf{x})}{h_j(\mathbf{x})}} \tag{2.3}$$

where $s_i(\mathbf{x})$ is the surface of the Voronoï cell face corresponding to the node $\mathbf{n_i}$ and $h_i(\mathbf{x})$ is the distance between point $\mathbf{x}$ and the node $\mathbf{n}_i$.

The method defined here is the Meshless Finite Element Method (MFEM) having both characteristics of a meshless method and of a traditional FEM. It is truly meshless because the shape functions depend only on the nodes position and the process of computing the empty spheres with four nodes and of generating all polyhedrical elements is bounded in time [7], but it is also a FEM because the space is divided into elements with continuity of the shape functions but discontinuity of the derivatives.

2.5 The boundary conditions

If sometimes there are boundary nodes explicitly defined as special nodes which are different from internal ones, in other cases the only available information is the total set of nodes and it is the algorithm that has to recognize the boundaries; this is exactly what happens with the Lagrangian formulation of fluid mechanics phenomena where, at each time step, a new node distribution is obtained and the free surface must be recognized from the node positions.

Introducing the value of the minimum distance between two nodes $h(\mathbf{x})$ and considering that it is a variable quantity, the following criterion is used: all nodes that are on an empty sphere of radius

$$r(\mathbf{x}) \geq \alpha h(\mathbf{x}) \tag{2.4}$$

are considered boundary nodes. α in 2.4 is a parameter close to, but greater than one. This criterion coincide with the *Alpha Shape* concept (largely treated in [9]).

2.6 The Particle Finite Element Method (PFEM)

All the problems to solve in traditional approaches have been pointed out and all the instruments to overcome them have been presented, last step is to put everything together to obtain an ideal method for fluid mechanic phenomena.

This is the Particle Finite Element Method (PFEM); its main features, already outlined in 2.2, can be briefly summarized in three big points:

- The information is particle based, i.e., all the geometrical and mechanical informations are attached to a particle;
- The MFEM is used to compute the force acting on each individual particle;
- The boundaries of the domain are defined using alpha-shape method.

PFEM can be seen as a particle method with special shape functions able to evaluate the interacting forces between particles, being a particle method it does not have problems in the definition of the boundaries that are determined by the particles themselves and not imposed by the problem, this means that the boundary contours are defined by the order h (where h is the distance between two neighbor particles). Furthermore the speed of generation of the mesh is of order n without degenerated elements and using MFEM, PFEM gains also all the other advantages of this approach as the ease to solve problems with variable h distributions or directional h distributions and conforming meshes.

Table 2.1 Comparison between different approaches

Problem	Standard mesh methods	Standard meshless methods	PFEM
Conforming	Difficult	Simple	Simple
Degenerated elements	Difficult	Simple	Simple
Boundary contours	Difficult	Difficult	Simple
Directional h	Simple	Difficult	Simple
Variable h	Simple	Difficult	Simple

Hence, if we summarize all the advantages and disadvantages of both mesh and meshless methods we can easily see in table 2.1 that all the different problems can be overcome with PFEM.

PFEM can be easily used in many applications but it is in problems with fluids with the presence of a free surface, breaking waves, or fluid domain separation, that it has the biggest advantages.

Fluid is assumed as incompressible and continuous when subjected to compression forces but it is able to separate under traction forces.

Boundaries are always modeled with an arbitrary number of particles; each particle is subjected to gravity forces and to forces due to the interaction between neighboring entities, that are calculates using the Navier-Stokes equations (as explained in chapter 1), this means that the mesh, once the forces are evaluated, become completely useless and it has to be re-build in the following step.

2.6.1 A full iterative time step

Knowing u^n and p^n as starting point, where n is the actual time step, the computation of the new particle position involves the following steps:

1- Approximate $u^{n+1'}$ taking the value of the last iteration if it is not the first one or assuming $u^{n+1} = 0$ if it is the first iteration;

2- Move the particle to x^{n+1} position and generate the mesh;

3- Evaluate u^* velocity. Being mass and stiffness matrix divided in 3 blocks, then the momentum equation has to be solved separately for u^*_x, u^*_y, u^*_z;

4- Evaluate the pressure p^{n+1} by solving the Laplacian equation;

5- Evaluate the velocity u^{n+1} and go to point 1 till convergence.

Chapter 3

Flip-buckets

3.1 Abstract

The aim of this chapter is to verify that the phenomenon of nappe detaching, due to the presence of a flip bucket with an angle of 30^o, is well reproduced using the *Particular Finite Elements Method* (PFEM) (see chapter 2). The jet trajectory along the jump, with particular care for the takeoff angle, and for the bottom pressure distribution along the upstream channel, are the first two parameters taken into account. A third parameter is controlled when a deflector is inserted as a restriction of the flow: the planar and side development of the shock wave that is created. We want to obtain a correspondence between experimental data on one side and output of the computational model on the other, trying to understand which are the main aspects that can influence the accuracy of the model and trying to overcome eventual problems of low congruence.

3.2 Introduction

Flip buckets are energy dissipators used at the end of ski jump spillway of big dams: the purpose of this structure is to throw the water well clear of the dam. The jet of a ski jump spillway leaves horizontally whereas the jet of a flip bucket is deflected upwards to induce disintegration in the air. Particular care should be taken in the construction of the landing area where the impact is surely strong. Moreover the spray produced can cause damage to the countryside and may adversely affect nearby electrical installations.

Figure 3.1 Schematic representation of a spillway flip bucket

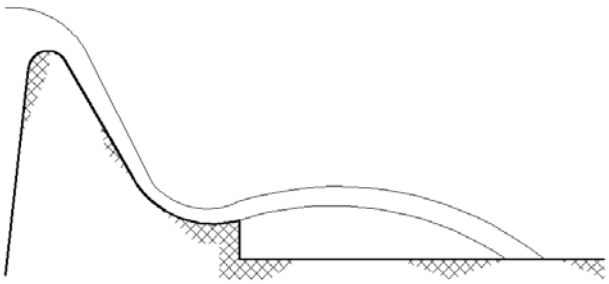

Figure 3.2 St.Mary's Dam, Alberta

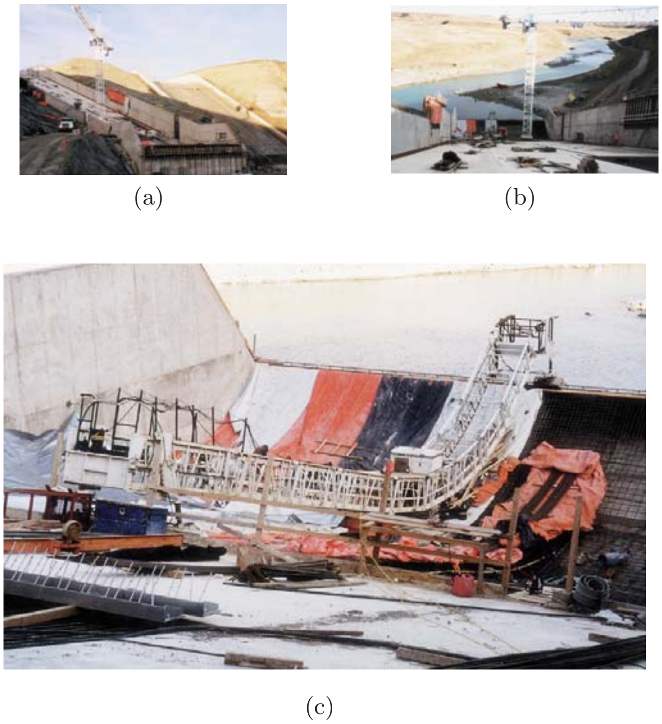

(a)

(b)

(c)

An example of flip bucket under construction can be the St. Mary's Dam, located approximately $40km$ southwest of Lethbridge, Alberta, that was built in 1951; now they are working to rebuild a new one as we can see in the photos of Fig. 3.2; another example the Shsta Dam Spillway in California (Fig.3.3)

Figure 3.3 Shasta Dam Spillway, California

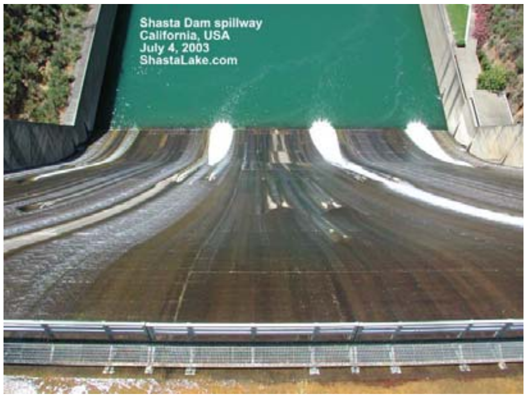

3.3 Experimental Setting

The experimental data taken to do a comparison with a computational model, are part of a research made by *Eng. Roman Juon* and *Prof. Willi H. Hager* [10] at the Zurich University.

The hydraulic experiments were conducted in a rectangular 7 m long channel, its base was 0.499 m and its height was 0.7 m. At the very beginning the flip buckets, composed of its 1 m long approach channel and its bucket of variable radius R and deflection angle β, was set.

Figure 3.4 Photo of the experimental set-up

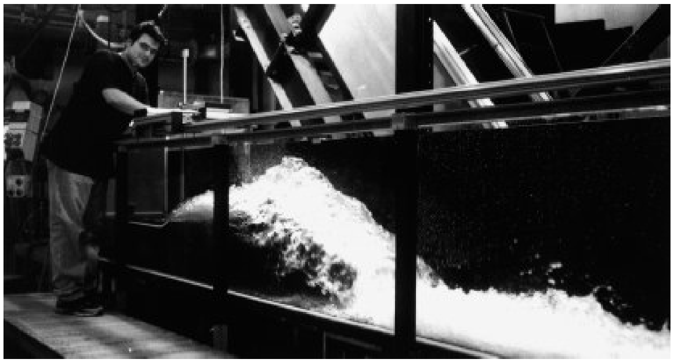

The discharge was controlled by a jet-box that could be regulated to obtain the flow velocity and the flow depth h_0 wanted. R was 0.25 m and the deflection angle was $\beta = 30^o$. The upper point of the flip bucket was

Figure 3.5 Schematic representation of experimental set-up: side

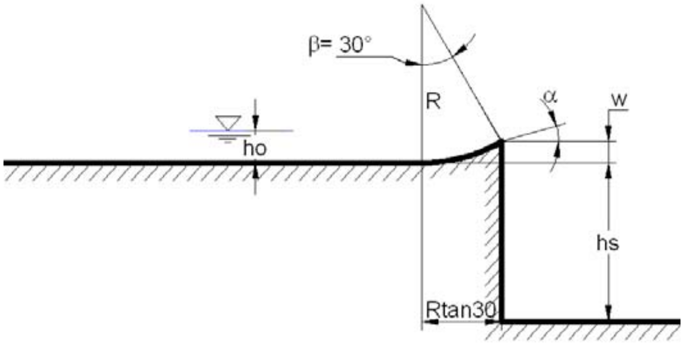

collocated $w + h_s$ upper than the downstream channel with $h_s = 0.25\ m$ and $w = (1 - cos\beta)R$ (bucket elevation). The determination of the free surface approach profile and of the upper and lower nappe profiles for the jet were made using a point gauge to ± 0.5 mm and ± 0.1 mm respectively.

The second part of the experiment included a 3D analysis: a deflector was collocated in the channel; it could be regulated starting from 0^o (the 2D case) until 30^o; the effect of the deflector was the creation of a shock wave as it will be analyzed in the following paragraphs.

Figure 3.6 Schematic representation of experimental set-up: plant

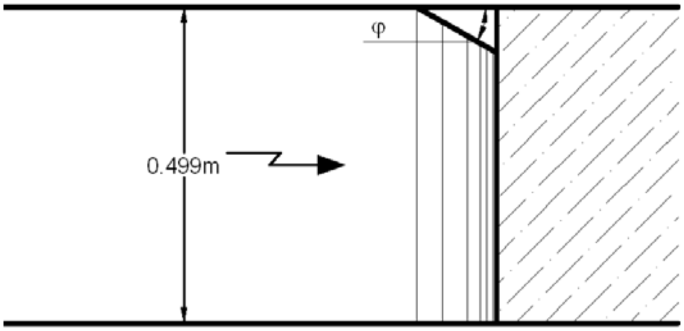

3.4 Experimental Results

Prof. Hager got many empirical functions which can describe the different aspects of the phenomenon, starting from its experimental data: the trajectory of the flow, of the waves, the developing pressure along the channel and so on; a brief overview follows of all these equations that are used for our validation.

The gathering of experimental data starts from different conditions of *Froude Number* that could vary from 3 to 7 and of depth of water h_0 that should be major than 4 *cm* to avoid scale effects.

Considering Prof. Hager [10] results it is possible to trace a qualitative jet trajectory of the upper and lower nappe profile from the takeoff point and of the pressure head distribution along the upstream channel.

$$z = z_0 + tan\alpha_j x - \frac{gx^2}{2V_j^2 cos^2\alpha_j} \tag{3.1}$$

The jet trajectories can be approximated with parabolas following the equation 3.1 where α_j is the takeoff angle, V_j is the takeoff velocity that can be considered equal to the approach velocity V_0 for flow conditions without scale effects. This equation takes origin from the classical equation of parabolic motion:

$$z = z_0 + tan\alpha_j x - \frac{1}{2}gt^2 \tag{3.2}$$

Instead of following a trajectory that maintain the initial take off angle, obviously the gravitational term acts correcting it; time is written as:

$$t = \frac{x}{V_j cos\alpha_j}$$

An important detail is that the take-off angle α_j is significantly smaller than the deflection angle $\beta = 30^0$ [11], and their ratio could be calculated in function of the ratio between the depth of the water and the flip buckets radius R

$$\frac{\alpha_0}{\beta}\left(\frac{70^0}{\beta}\right)^{\frac{1}{6}} = \frac{1}{2}\left[1 + exp\left(-8\left(\frac{h_0}{R}\right)^2\right)\right] \qquad for \qquad 0 \le \left(\frac{h_0}{R}\right) \tag{3.3}$$

The second parameter taken into account in this study is the pressure

Figure 3.7 Qualitative jet trajectory

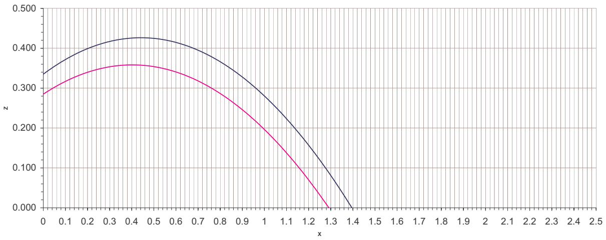

(h_P) that develops along the upstream part of the structure used for the experiment: therefore pressure has to be constant on the approach channel and constantly equal to $h_P = h_0 = 0.05\ m$ from one side and it has to be equal to the sum of a static pressure head (h_0) plus a dynamic portion on the flip bucket on the other side. The dynamic part has to be different than 0 only on the flip bucket. Taking into account the normalized parameter:

$$H_P = \frac{h_P - h_0}{h_{PM} - h_0}$$

where the abscissa origin, $x = 0$, is located at the take off point and $R \cdot sin\beta$ is the flip-bucket length, h_{PM} is the maximum pressure head plotted along the normalized streamline coordinate $X_P = \frac{x}{R \cdot sin\beta}$, and can be calculated as $\frac{h_{PM}}{h_0} = (\frac{h_0}{R})F_0^2$ thinking of having a potential vortex model, this assumption is correct if the Bend number $B = (\frac{h_0}{R})^{0.5} F_0 \leq 1.5$; the development of H_P should be:

$$H_P = [-2X_P \cdot exp(1 + 2X_P)]^{\frac{2}{5}} \tag{3.4}$$

The changing of precision in the 2D computational output is analyzed considering:

- the refinement of the meshes.
- the changing of the discharges *Froude Number*;

In the second part of the experiment we analyze the effect of a deflector of variable angle posed at the bucket beginning: a shock wave is generated, its maximum height should be more or less twice the maximum nappe height without deflector, and its planar contraction should occupy all the channel in function of the angle.

Figure 3.8 Qualitative bottom pressure distribution

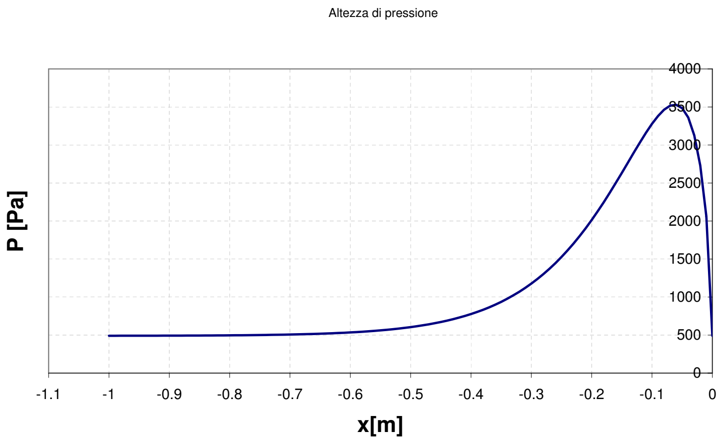

The shock-wave profile was described by Hager [10] with the profile of a standard spillway:

$$X^* = A(X_L + B); \tag{3.5}$$

$$Z_L = -\frac{X^*}{C} - D. \tag{3.6}$$

Where, for the specific case, $A = 0.14$, $B = 2.7$,$C = 0.023$ and $D = 16$.

$$X_L = \frac{x}{h_0 F_0}; \tag{3.7}$$

$$Z_L = \frac{(z_L - z_{LM})}{h_0 sin^{\frac{3}{8}}\varphi}. \tag{3.8}$$

With z_{LM} maximum nappe elevation that, as x_{LM}, depends only on the approach *Froude Number*:

$$\frac{x_{LM}}{h_0 F_0} = 0.05 F_0^2; \tag{3.9}$$

$$\frac{z_{LM}}{h_0 sin^{\frac{3}{4}}\varphi} = 0.45 F_0^2. \tag{3.10}$$

Figure 3.9 Qualitative shock-wave trajectory

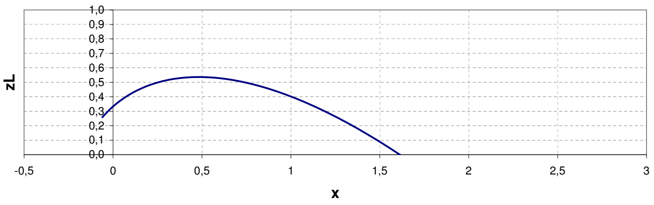

3.5 2D Model

Using *GiD program* [1] it has been built a simple two dimensional model that reproduced the experimental setting. The approach channel was only 1 m long because it is proved that flip buckets effects can be considered negligible for $x \leq -0.5\ m$ on the contrary the downstairs channel is 1.5 m for the lower *Froude Number* such as 3 and 4, and 2.5 m for *Fr* 5 and 7. Only two layers have been necessary to generate the complete geometry and these layers due to correspond to two big group set inside *PFLOW program*:

-Solid : being the structure a fixed one, the best constrain to impose to it, is the velocity equal to zero ($v_x = 0, v_y = 0, v_z = 0$). *ALE* is its system of reference [3] and this means that the fluid can be analyzed considering a Lagrangian or Eulerian approach: the nodes of the computational mesh can respectively follow or not the continuum or can be moved in some arbitrarily way to permit a rezoning capability, as explained in appendix A. This particular choice of description of motion is due to the fact that in such a simulation the structural part is subjected to interaction with a fluid, that is, it is the zone where the higher relative difference of velocity is registered between points. This means that if we use a lagrangian description, then elements distortions will be too big, or, to avoid this, δt of integration will be too small and so computationally heavy.

-Fluid-in : a fluid that is created from a linear element which is the *ALE* way to create an incoming flow; the line is considered lagrangian, whereas the other nodes, as soon as they “detach” from the line, become ALE; only the free-surface is fully lagrangian.

Water is the considered fluid for all the analyzed experiments; its physical characteristics are:

- Density : $1000\frac{kg}{m^3}$
- Dynamic viscosity : $10^{-3}\frac{Ns}{m^2}$
- Inflow velocity : changing its x-component in function of the *Froude Number*

Figure 3.10 Experimental jet trajectory

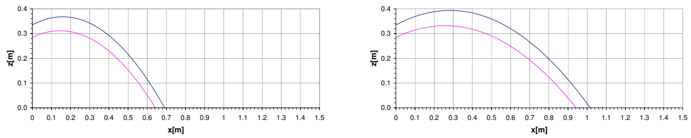

(a) *Fr=3* (b) *Fr=4*

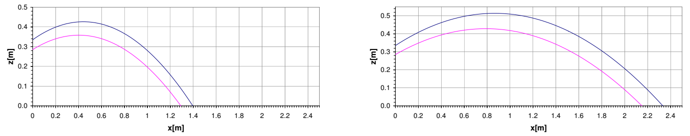

(c) *Fr=5* (d) *Fr=7*

Table 3.1 Discharge datos for the 4 models

Model	Fr	Q $[l/s]$	v_{in} $[m/s]$
a	3	52.41	2.1
b	4	69.88	2.8
c	5	87.35	3.5
d	7	122.29	4.9

Basically two different kind of meshes have been considered for each *Froude Number*, keeping constant the depth of the inflow discharge equal to 5 *cm*; the first mesh is 1 *cm* large, the second one is 0.5 *cm* large; the models initially have respectively 831 and 1659 linear elements; a shorter model was sufficient in the case of the slowest discharges ($Fr = 3$ or 4) because the jet touched the channel after less than a meter as we can see in fig. 3.10,so the meshes are less heavy: respectively 631 and 1259 elements.

It is necessary to think that the complexity of the mesh grows with time because of the creation of the fluid thetraedra incoming the model and that some conditions, set into the initial model, may change: for example fluid velocity, that was imposed building the geometric model, would not be the velocity of the jet in any time and this can imply problems with the choice of the Δt of integration; in fact relative velocity between elements multiplies by the smallest Δt of integration has to be smaller than the dimension of the generated mesh. This aspect can create some problems when, in the jump, the kinetics energy takes the place of the potential one in an energy balance. Some implementations of both the 2D and 3D models stopped at a certain point because of this excessive largeness of time interval that did not permit to capture any good solution.

3.5.1 Jet trajectory

Considering the velocity of the discharges (Tabular3.1) the output of the model after 1 *second* and after 2.5 *seconds* is analyzed to be sure that a state that can be considered a steady one is established.

Figure 3.11 *Froude Number* 3: comparison between graphical computational output and experimental interpolating function

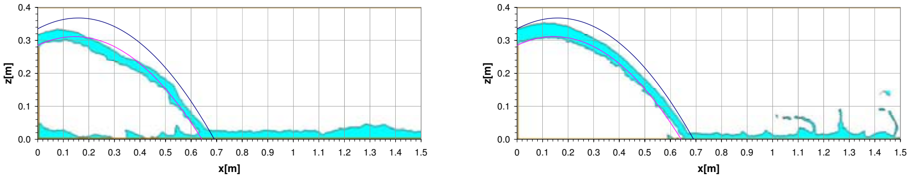

(a) 1 *cm* mesh (b) 0.5 *cm* mesh

Figure 3.12 *Froude Number* 4: comparison between graphical computational output and experimental interpolating function

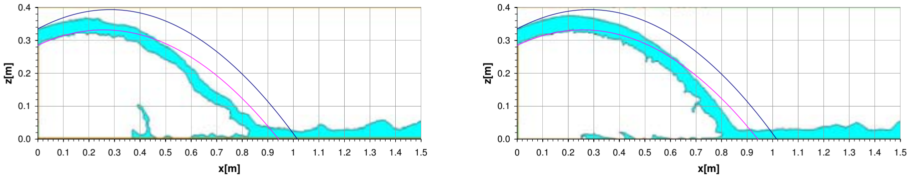

(a) 1 *cm* mesh (b) 0.5 *cm* mesh

As expected the accuracy of the output jet trajectory improves with:

- the refinement of the mesh;

- the increasing of the velocity.

Figure 3.13 *Froude Number* 5: comparison between graphical computational output and experimental interpolating function

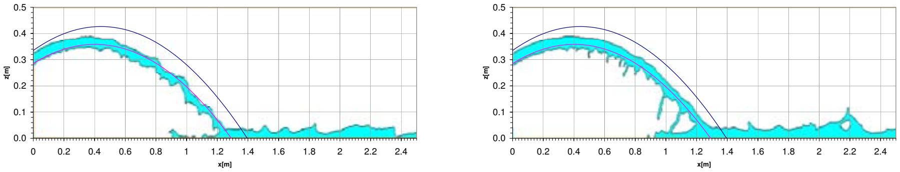

(a) 1 *cm* mesh (b) 0.5 *cm* mesh

Figure 3.14 *Froude Number* 7: comparison between graphical computational output and experimental interpolating function

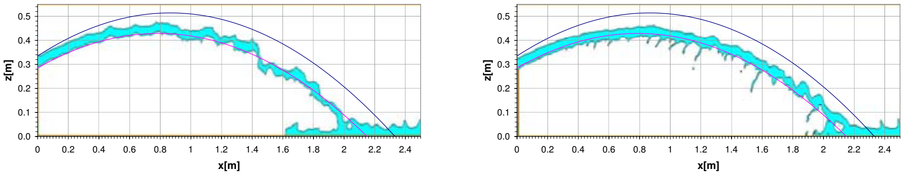

(a) 1*cm* mesh (b) 0.5*cm* mesh

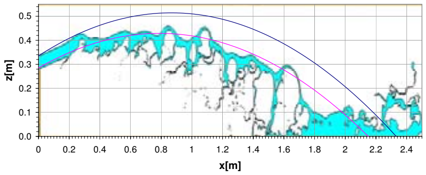

(c) 0.5*cm* mesh

Figure 3.15 side view to flip bucket flow

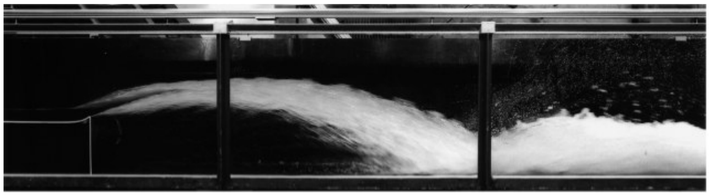

It is built a mesh of 0.2 *cm* long linear elements, for the discharge with *Froude Number* 7, that seems the one that better reproduces the theoretic phenomena: a very heavy model, being a 4150 elements mesh only at the beginning, which took more than two weeks to be implemented without giving good results. In fact the accuracy that increases between the 1 *cm* mesh and the 0.5 *cm* mesh degenerates with the third one, as it can be seen in fig. 3.14: we cannot say that it was a computational problem, in fact, thinking at the physical phenomena (Fig. 3.15), the nappe profile tends to open itself: therefore it becomes hard to analyze the results being impossible to follow the profile. For sure a big loss of mass is present: this problem is due partly to the same *alpha-shape* method and partly to the numerical approximation in the incompressibility constraint where a Laplacian operator is used, knowing that this kind of operator would be correct in the continuum case, not in he discrete one.

Figure 3.16 1 *cm* mesh

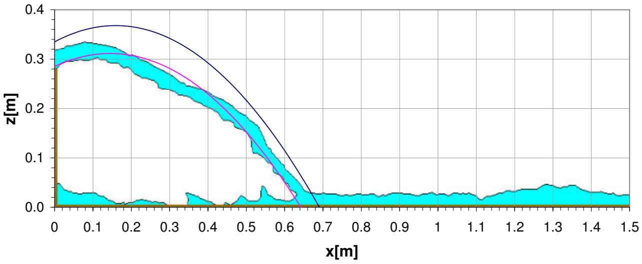

(a) Dopo 1 *sec*

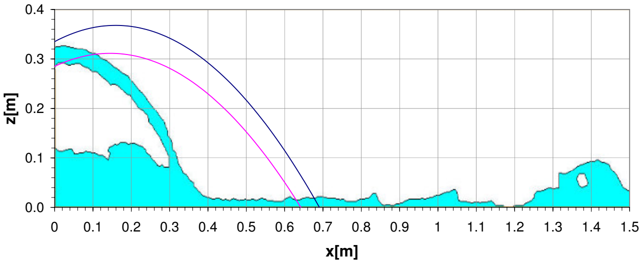

(b) Dopo 2.5 *sec*

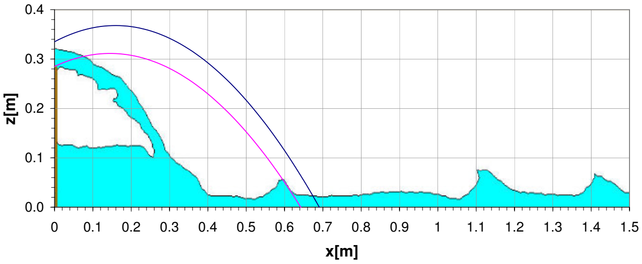

(c) Dopo 4 *sec*

The precision of the program is higher with the increasing of the velocity. The biggest problems occur in the case of *Froude Number*= 3: experimental results are completely different from computational one, once the steady state is set. The flow seems not to have the energy to keep the jet active.

In this prticular case a big difference can be noticed between the contact moment and any other moment in the steady state as in fig. 3.16. This problem was subdued passing from the 1 *cm* to the 0.5 *cm* mesh, as shown in fig. 3.17. Usually the difference between the contact moment and an instance in which the steady state is set, has a negligible entity, but the touching point is always a bit farer from the flip bucket in the first case.

Once the jet touches the downstream channel, part of the water tends to continue the flow, but part tends to fill the zone under the jet, creating a stagnation. We built a model with a little inclination of the approach zone to look if something would change giving an impulse to the water to continue

Figure 3.17 0.5 *cm* mesh

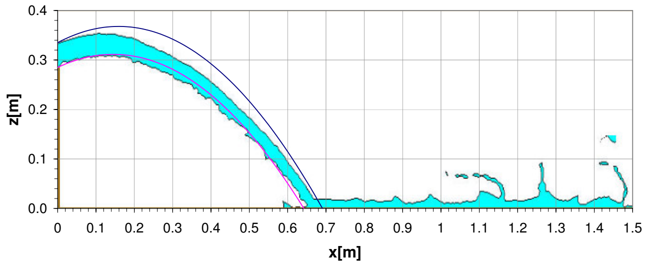

(a) Dopo 1*sec*

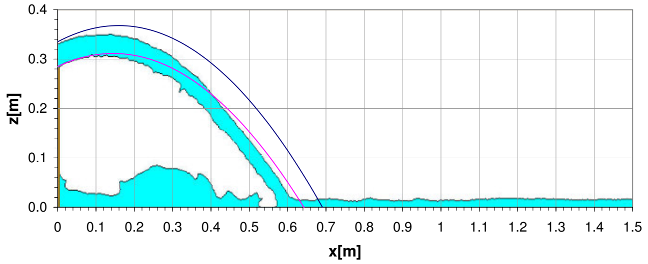

(b) Dopo 2.5 *sec*

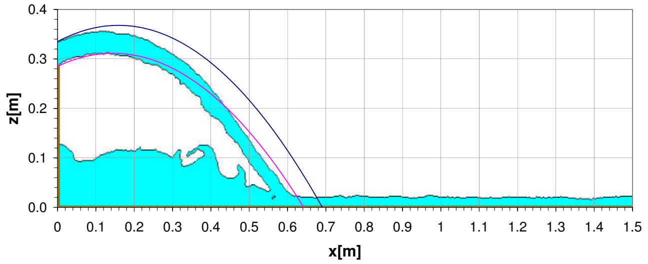

(c) Dopo 4*sec*

Table 3.2 Precision in the touching point

		x Lower Profile	x Upper Profile
Fr=3			
	Theoric Model	0.642	0.691
	1 *cm* mesh	0.315	0.345
	Error	51%	50%
	0.5 *cm* mesh	0.595	0.645
	Error	7%	7%
Fr=5			
	Theoric Model	1.292	1,396
	1 *cm* mesh	1.145	1.275
	Error	11%	9%
	0.5 *cm* mesh	1.276	1.395
	Error	1%	0%
Fr=7			
	Theoric Model	2.205	2.332
	1 *cm* mesh	1.975	2.055
	Error	2%	12%
	0.5 *cm* mesh	2.185	2.295
	Error	8%	2%

flowing in a single direction; no important differences can be noticed.

Figure 3.18 Initial perturbation

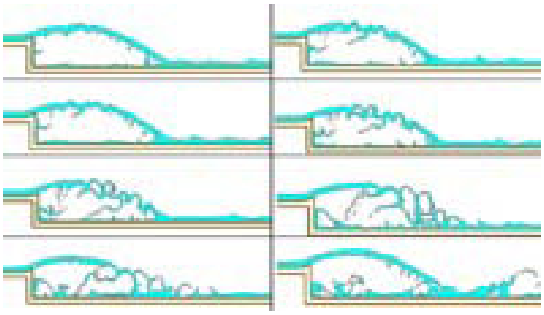

This returning wave, in the model with *Froude Number*= 5, has too much energy at the beginning if compared with the height of the jump in fact it perturbs the trajectory of the flow as shown in Fig. 3.18. It is only a transient phenomenon, due to the major energy of the initial flow; the accumulated water smoothed this energy of the back wave after a few seconds and the problem does not occur any more.

3.5.2 Pressure

Looking at the output of the bottom pressure distribution and comparing the results obtained in the graphs with the qualitative tangle of the experimental results the differences were not negligible. Along the approach channel, as already said, the pressure head should be constant and equal to the depth of the flow; looking at the graph there are continuous oscillations around the correct value of pressure. This is something acceptable because oscillations are always present also in experimental observations and because we are analyzing a discrete model, not a continue one.

Along the flip-bucket the increasing of the dynamic head contribution did not follow the same behavior. In fact, watching what happenes between 30 and 10 *cm* before the take off point, it arrives at differences of pressure of about 40-45%. The only entity that is well reproduced is the top of the pressure head as we can see in the following figures.

Also in this case the increasing of the velocity helps the precision and the model with a discharge with *Froude Number* = 3 gave more problems (Fig. 3.20). The passing from a 1 *cm* mesh, to a 0.5 *cm* is not a solution: if the first mesh gives lower level of pressure (more or less $\frac{2}{3}$of the experimental value), the second one overcomes the higher pressure head also of a 10%. These problems are not present with the other discharges and the passing from a larger mesh to a thiner one permits a bigger accuracy, but the difference is not really relevant for this particular velocity. The model with *Froude Number* = 7 gives a very precise level of maximum pressure head, nearly exact, but the phase of increasing of the dynamic pressure had the same problem of all the other meshes.

Figure 3.19 *Froude Number* 3 after 4 *sec*

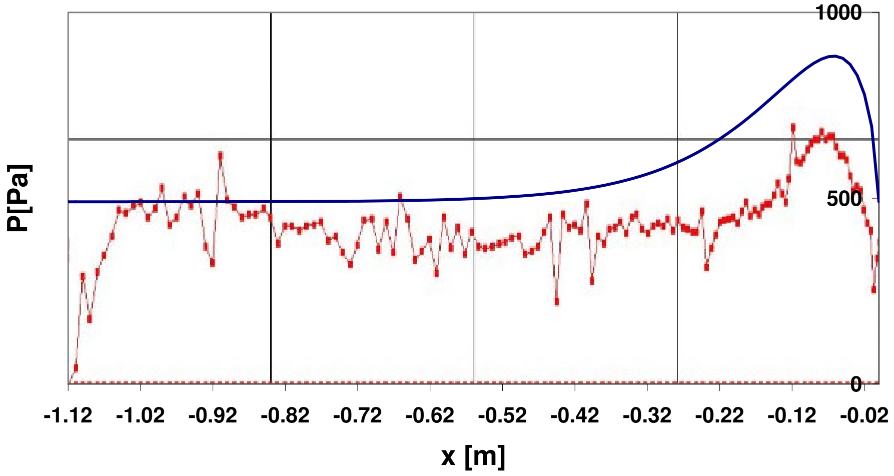

(a) 1 *cm* mesh

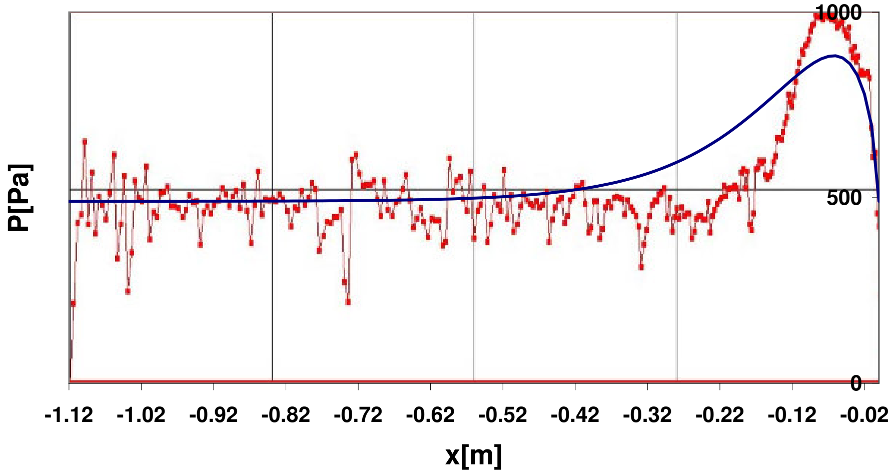

(b) 0.5 *cm* mesh after

Figure 3.20 *Froude Number* 3 after 5 *sec*

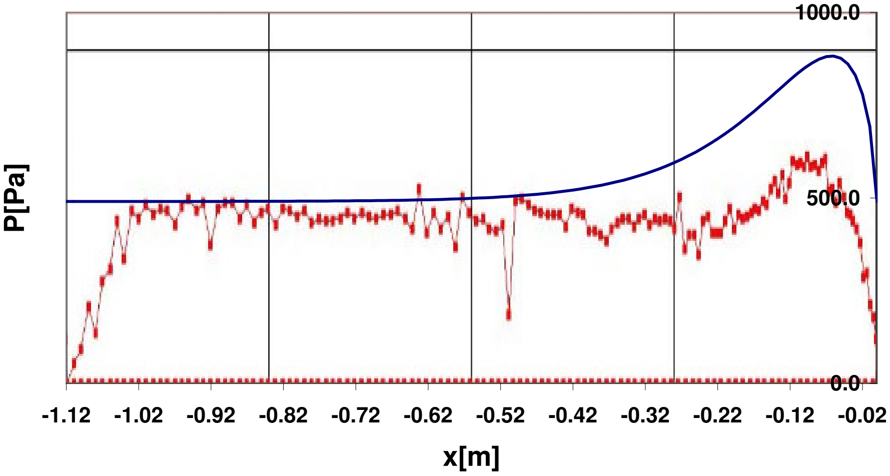

(a) 1 *cm* mesh

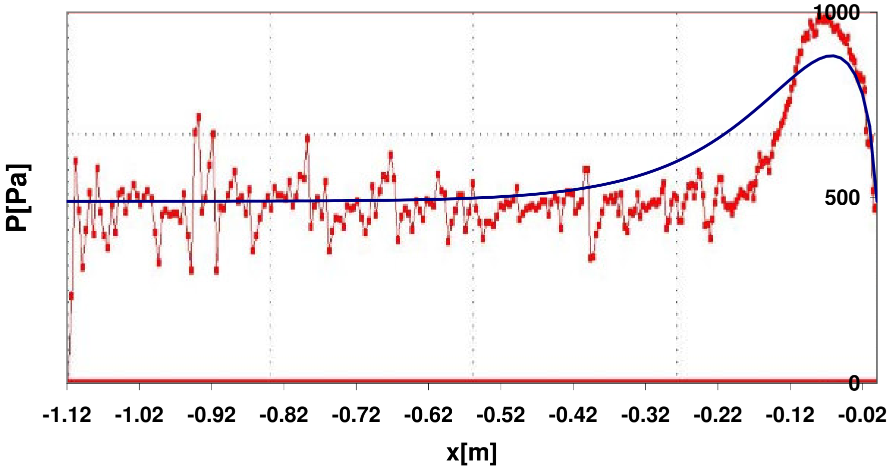

(b) 0.5 *cm* mesh

Figure 3.21 *Froude Number* 5 after 5 *sec*

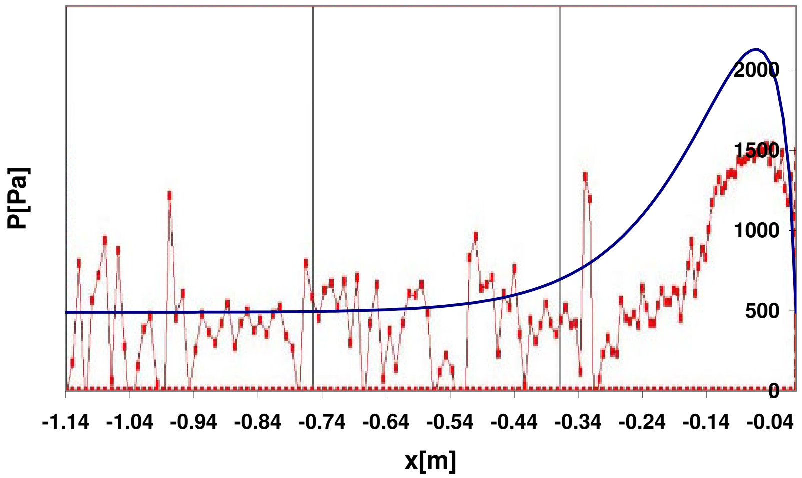

(a) 1 *cm* mesh

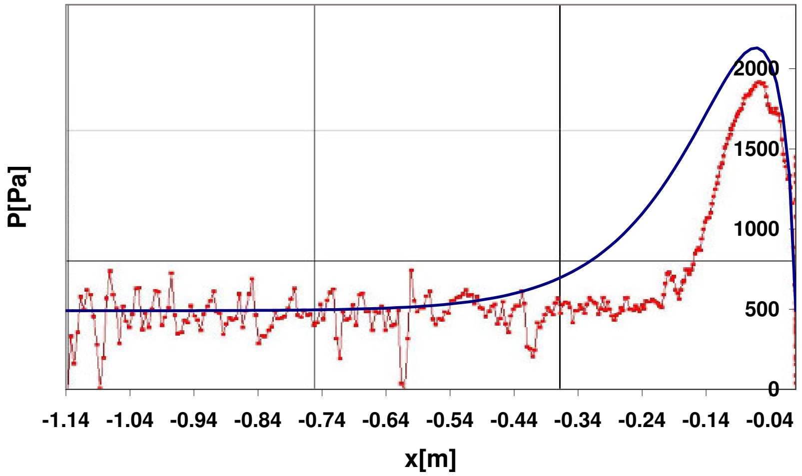

(b) 0.5 *cm* mesh

Figure 3.22 *Froude Number* 7 after 4 *sec*

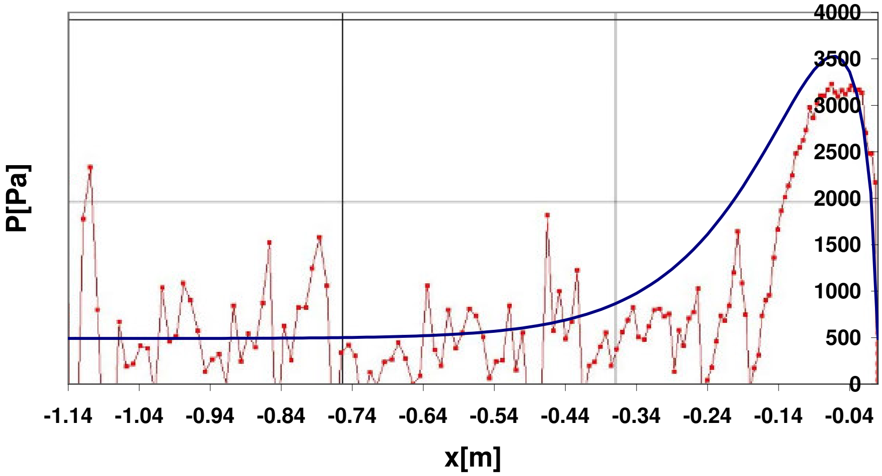

(a) 1 *cm* mesh

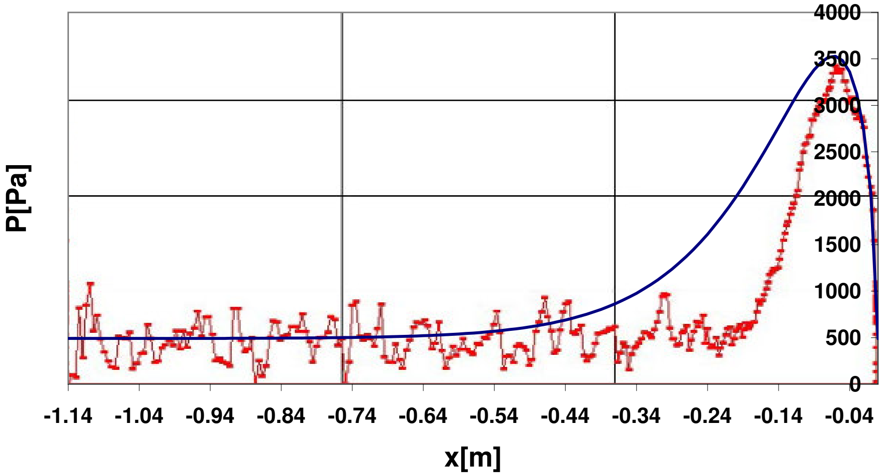

(b) 0.5 *cm* mesh

3.6 3D Model

Figure 3.23 3D experiment

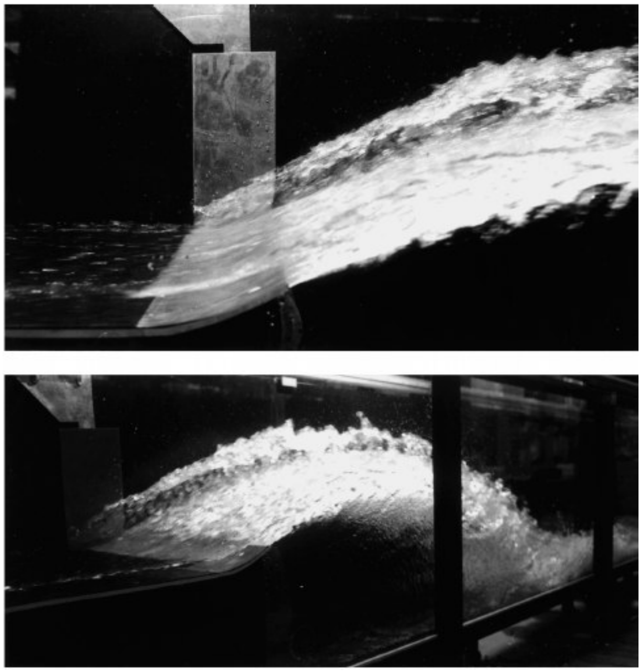

Figure 3.24 Shock-wave

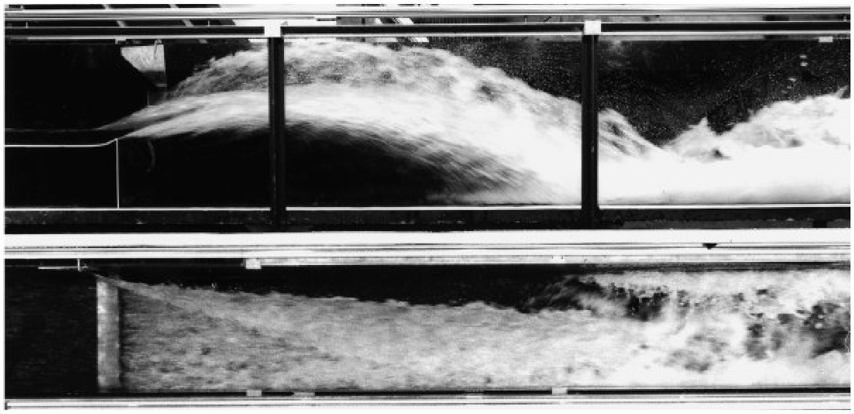

The second part of Prof. Hager [10] experiment considered the effect of a deflector of variable angle (β could vary from 0^o to 30^o) that created a

Figure 3.25 Geometry

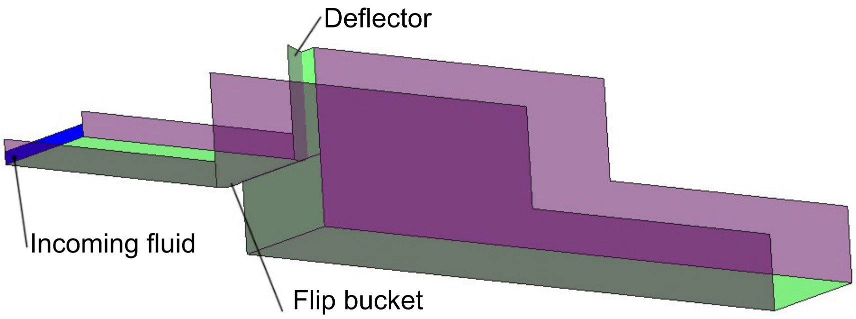

restriction of the channel over the flip-bucket (fig. 3.23 3.24. A 3D model is built using surfaces that reproduces the geometry of the entire experimental setting as it can be seen in fig. 3.25.

The plane and side development of this wave is the parameter analyzed in this section. The main problem with this kind of model is the presence of an incoming fluid: the initial mesh is composed of more or less 72000 triangular elements that increase after very few seconds of processing, arriving also at 1.5 million of elements; this means that the model becomes very heavy and only a $\Delta t = 0.04 sec$ can be achieved in an entire day of processing. Time necessary to have concrete results is really too much to permit the implementation of all the different cases of the 2D analysis: one model for each Froude Number has been built with a constant mesh dimension of $\Delta x = 0.01 cm$.

Two side of the shock wave are analyzed: the $X - Y$ and the $X - Z$ trajectory, as already said in 3.4. It was quite hard to extrapolate clear images from the output because the phenomenon of the development of such a wave it is not isolated from the flux but it is part of it.

As we can see in the following figure the side development of the shock wave is really well reproduced from the model, also in direct comparison with the photos of the experiment. It is more difficult to see the good simulation of the planar trajectory that can be only qualitative. In any case the expected behavior is confirmed.

Figure 3.26 Fr5

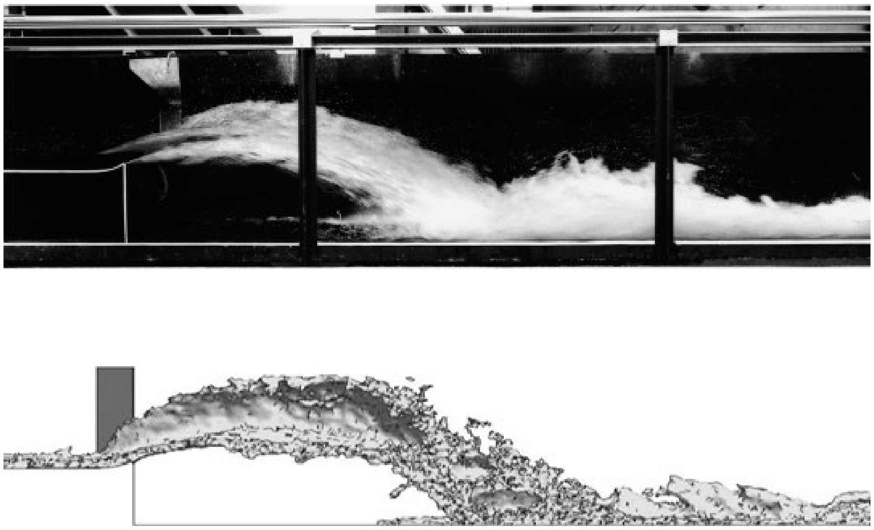

Figure 3.27 Fr 5: side development of the wave

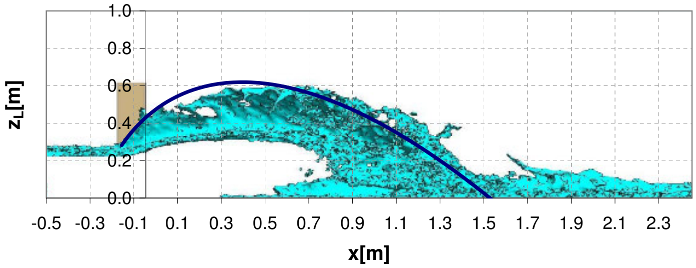

(a) After 1.32*sec*

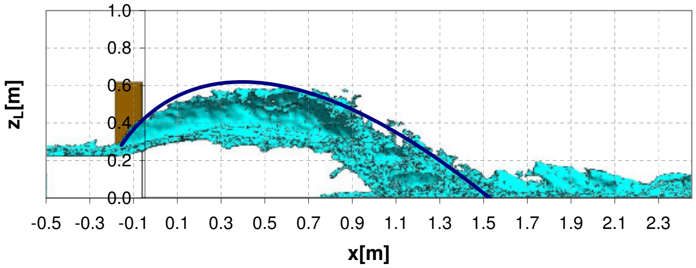

(b) After 1.48*sec*

Figure 3.28 Fr 3: side development of the wave

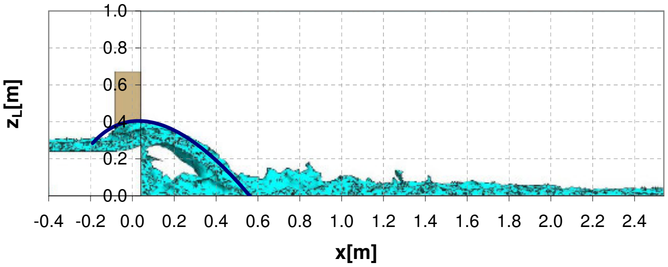

(a) After 1.32*sec*

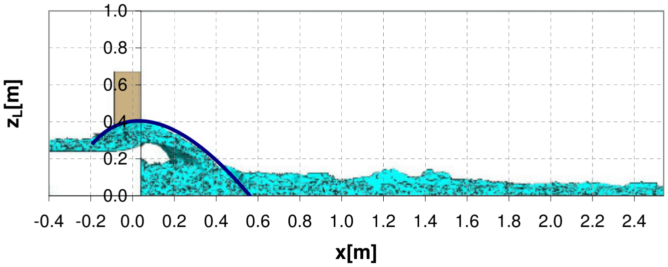

(b) After 1.48*sec*

Figure 3.29 Fr 5: planar development of the wave

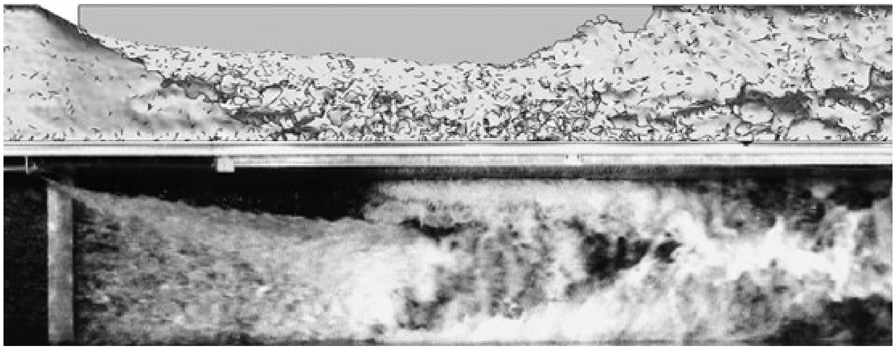

Figure 3.30 Fr 7: planar development of the wave

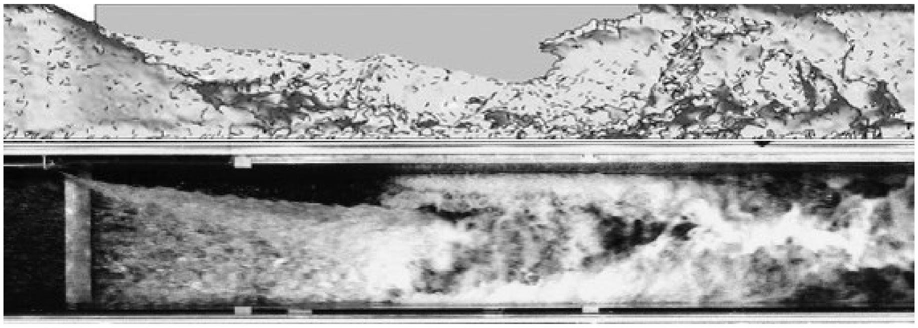

Chapter 4

Sluice gate

4.1 Abstract

This chapter presents an other example of hydraulic phenomena. The aim of this work is that of reproducing the under seal outflow in presence of a sluice gate: a passage fitted with a vertical sliding gate used to regulate the flow of water in a channel or lock. The parameters which are going to be analyzed are pressure on the gate and the vena contracta which should follow theoretical and experimental data. In a second moment we try to reproduce an hydraulic jump analyzing the loss of energy and the change of flow depth.

4.2 Introduction

One of the typical and mostly used discharge regulator is a sliding gate which can control the outflow of water. Speaking of shape and dimensions we can find a lot of example starting from the gates that are at the two extremes of a chamber and arriving at the most common use of them to garrison the discharge channel of a dam.

The discharge of the under seal outflow is governed by the classical equation:

$$Q = a \cdot C_c \sqrt{2gh} \tag{4.1}$$

where a is the height of the sliding gate, $C_c = 0.611$ is the contraction coefficient and h is the depth of upstream water. The distribution of pressure along the gate should be more or less hydrostatic growing proportionally with the product between depth y and specific weight γ: $P = \gamma y$. And the behavior of the outflow discharge and the nappe contraction is analytically described and experimentally proved once the upstream condition and the geometrical data are given. The aim of this work is to verify the coherence between this description and the computational output. The length of the model and that of the experimental channel in this case, as usually, is not sufficient to see the establishment of the real downstream conditions with the changing from a fast to a slow flow, to do that, and to analyze the hydraulic jump that will create we introduce a notch fall to oblige the flow to increase the depth of water to gain the sufficient energy to overcome it passing in this case to a slow flow. The control of the two corresponding depth [5] of the hydraulic jump and of the velocity of the slow and fast flow can be done both with numerical approach and with experimental data.

4.3 Experimental setting

Figure 4.1 Schematic representation of the experimental apparatus

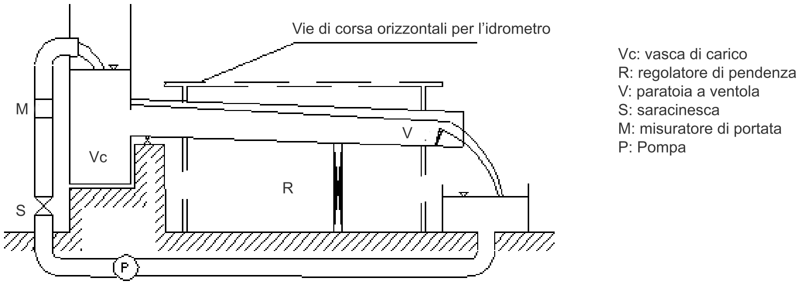

The experimental data used for the comparison in the current chapter, are taken from the laboratory experience of a group of students of the hydraulic section of the faculty of civil engineering of the University of Padua.

The experimental apparatus is schematically represented in fig. 4.1 and it is composed of a plexiglas rectangular channel, its length is 1 m and its width is 0.3 m. This channel leans on a beam that can be regulated to simulate different inclinations. Upstream the channel there is a big tank that is the source of the inflow discharge and that controls its regulation. Downstream the channel there is an other tank where water falls in; an electrical pump permits the passage of water from the downstream reservoir to the upstream one as to create a closed circuit with constant discharge. At the end of the channel there is a valve blade that can be regulated to create the downstream conditions wanted. Sixteen pressure intakes are connected with some absolute piezometers, seven of them are inserted in the sluice gate the other on the bottom of the channel.

4.4 Model

Figure 4.2 Sluice gate: a detail

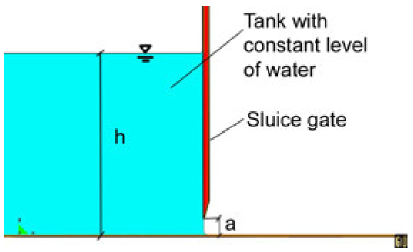

The necessary model we have to build to reproduce the structure is a 2D one, in fact the phenomenon of flow under seal has ever been studied as a 2D one being the width of the analyzed channel, usually much bigger than the height of the sluice gate and therefore of the depth of the outing flow.
The geometry of the solid part is really simple, the only real part to take care on is the gate that is 1 *cm* thick and it is thiner in the lower part where it ended as shown in fig. 4.2, the contraction coefficient can vary a lot in function of the shape of the lower part of the sluice gate because of the influence on the outing discharge. What it was more difficult to create, it was the reservoir in fact, we know that the under seal flow is regulated from one side by geometric aspects and from the other side, more important in this case, by the depth of the upstream water in the tank. All this can be seen in the following equation of under seal flow.

$$Q = a \cdot C_c \sqrt{2gh} \tag{4.2}$$

where a is the height of the gate in respect with the bottom of the channel and C_c is the contraction coefficient that Kirchhoff demonstrated that, in the case of a plane vertical gate, if this last one is lifted up of a quantity which is much smaller than the width of the same, it can be calculated as

$$C_c = \frac{\pi}{2+\pi} = 0.611;$$

On the other side there is a dependence by the depth of the upstream water that is supposed to be quiet being a tank with constant volume from a theoretical point of view , but because in reality it is not as big to permit this hypothesis being an other piece of channel where a constant discharge is put in, we have to find a way not to perturb the free surface too much. With the help of GiD [1] we can easily draw a fluid volume, the difficult part is to find out a way to balance from one side the under seal discharge destined to go away because of gravity force, and from the other side, the same discharge that we put inside without causing big perturbations.

Figure 4.3 Different models for the tank

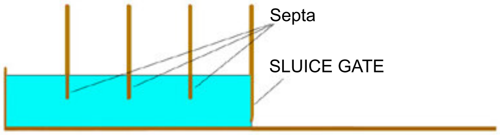

(a) 1^{st} model: Septa

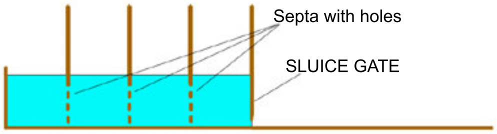

(b) 2^{nd} model: Septa with holes

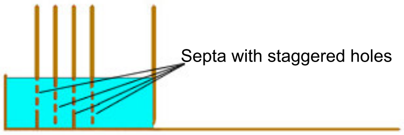

(c) 3^{rd} model: Septa with staggered holes

The ideal solution seems to be to impose the condition of initial velocity to the vertical line at the left extreme of the model (fig.4.7(a)) that has

Figure 4.4 Different moments of the simulation: 1^{st} model

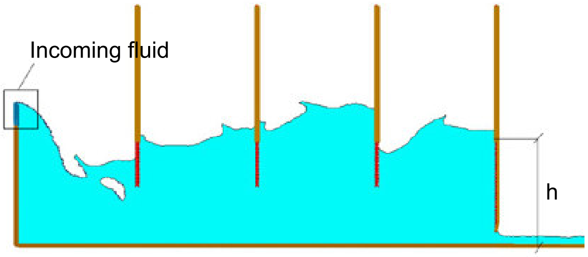

(a)

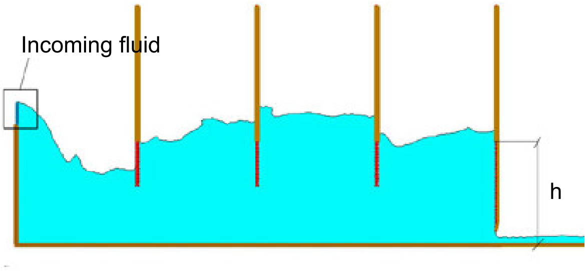

(b)

the height of the depth of water wanted for the upstream discharge and to impose that the flow will be created from that line pulling the mass of fluid forward and arriving quite soon to a steady state. The theoretical hypothesis of a infinite tank of constant level would be respected in this case. The vertical line at the extreme left is supposed to be Eulerian so that the fluid can advances whereas the computational mesh is fixed: this is one of the two way to obtain a creation of fluid.

The other one implies the use of a *fluid-in* with Ale condition of motion but does not hallow the line, from which the fluid is created, to have nothing in front of it (fig.4.7(b)), otherwise the process will stop because of the impossibility of creating element, it will be the same of having a wall in front of the line from which the flux is created. We finally used the second one because of many problems arisen with the model using the first way, in fact the discharge taken into account were probably too slow, as to say that the velocities were too small to permit a good working of the program that still does not work very well with slow discharges (*Froude Number* ≤ 1).

Using the Ale condition of motion, we have to put the "fluid-in line"

Figure 4.5 Different moments of the simulation: 2^{nd} model

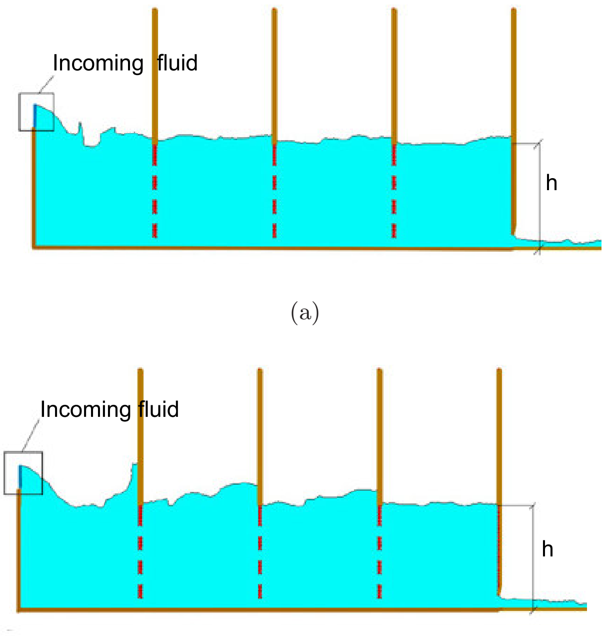

(a)

(b)

above the surface that represents the fluid and we simulate the entrance of a flux directly falling into the water of the tank. This is the reason why we have to introduce many septa to try not to have a perturbed flux; this is not sufficient alone, in fact the first models continue to see wave creation as we can see in fig. 4.4 and the situation gets a bit better introducing a series of holes in each septum (fig. 4.5). The best results are obtained with the introduction of septa with staggered holes (fig. 4.6).

The first two models (fig.4.4, fig.4.5) have been used to verify the good behavior of the under seal flow, three parameters have been analyzed:

- The pressure along the gate;
- The outing discharge;
- The analysis of the free surface of the downstream water;

The discharge used in the laboratory for the experiment was $Q = 31\ l/s$; the the sluice gate was raised from the bottom of the channel of $a = 6\ cm$.

Figure 4.6 Different moments of the simulation: 3^{rd} model

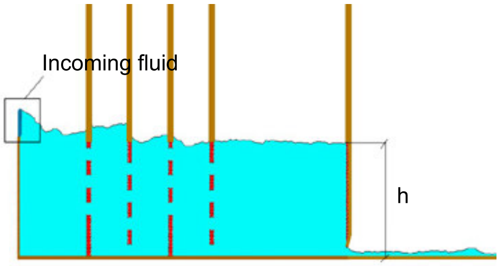

(a)

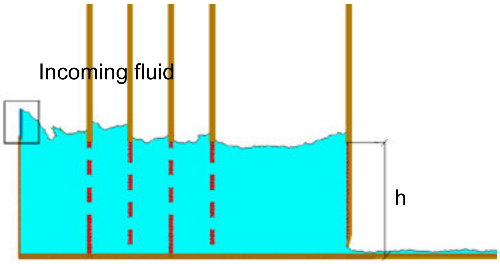

(b)

The dimension of the mesh of the model is $\Delta x = 1\ cm$. The depth of the water in the tank, following the 4.2 was $h = 0.433\ m$.

The last model has been used to verify the possibility of catching a localized phenomenon like the hydraulic jump that is generated, as we know, by the clash of an upstream fast discharge, with a downstream slow discharge. In our model, as during the experiment, these boundary conditions are created by the simultaneous action of the sluice gate that creates a fast discharge (*Froude Number* $\geq$ 1) and to the presence of a step at the right side of the model, that, representing an high step for the considered flow, generates a transition from fast to slow flow to gain energy to pass the obstacle [12]. In this case the discharge of the model is $Q = 21.1\ l/s$ and the sluice gate is raised from the bottom of the channel of $a = 4\ cm$. The dimension of the mesh is $\Delta x = 0.8\ cm$. The depth of the water in the tank, following the 4.2 was $h = 0.422\ m$.

Figure 4.7 Different possible models

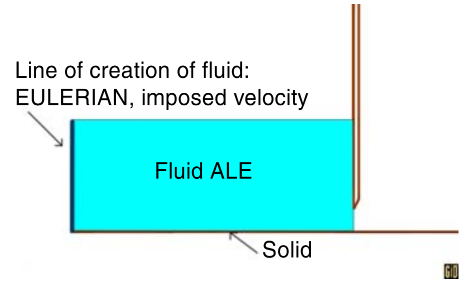

(a) Eulerian representation

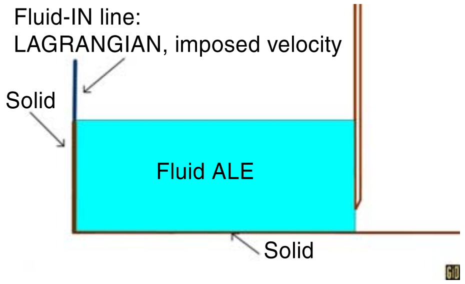

(b) ALE representation

4.5 The pressure along the gate

Taking into account an irrotational fluid, the energy presents into the stream tube can be considered constant, this means that because of the growing of velocity in the zone near the sluice gate, pressure head has to reduce itself drastically if compared with the hydrostatic value.

The measurements made at the University of Padova were conducted using 7 piezometers on the sluice gate as we can see in fig. 4.8, knowing from the beginning the value of the capillary migration: it was equal to 4.43 mm, calculated using Jurin equation [12]

In fig 4.10 and 4.11 the comparison between experimental results (the red line in the graph, with the underlined points which are the measured one) and the computational output, given by a *line graph* by GiD post-process options (the blue line), is printed for different instances in the two models taken into account and described in 4.4.

As we expected, the analysis, in the case of the model with septa with holes (2^{nd} one) gives an upstream depth that is more regular and less subjected to waves due to incoming flow, and this fact allows a very good

Figure 4.8 Piezometers

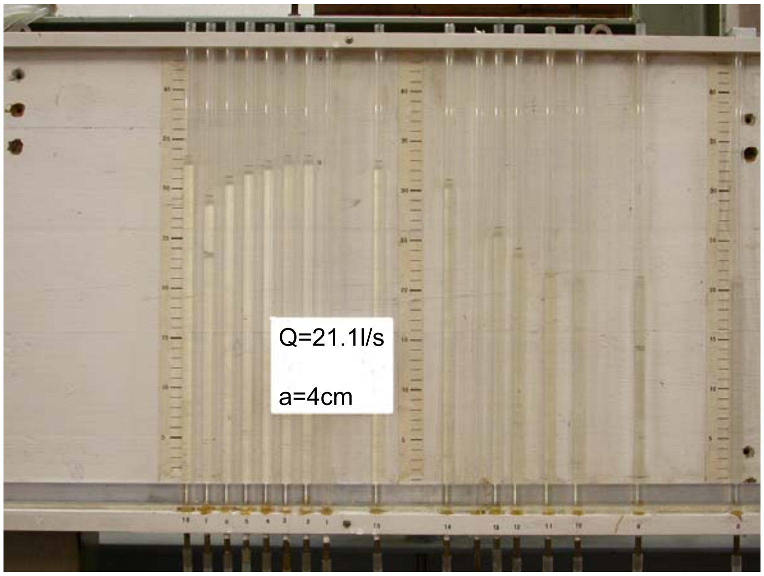

Table 4.1 Experimental results: pressure head for $Q = 31\ l/s$

Piezometer	h $[cm]$	h =h−4.43 mm $[cm]$	z $[cm]$	$h - z = P/\gamma$ $[cm]$
1	43.7	43.3	34.20	9.06
2	43.4	43.0	19.20	23.76
3	42.7	42.3	9.20	33.06
4	41.1	40.7	4.20	36.46
5	39.4	39.0	2.60	36.36
6	35.8	35.4	1.20	34.16
7	30.0	29.6	0.48	29.08

comparison with the experimental results as we can see in fig. 4.11 On the contrary, looking at the results of the 1^{st} model, that one with only septa, the dynamic effect increases the value of pressure head as we can see in fig. 4.10 *a* and *b*; this is a consequence of the presence of a dynamic effect which cannot be negligible, only studying an output of an instance in which the upstream depth is quite regular the pressure head development is as good as the one of the other model.

As clear in fig. 4.12, looking at the variation of pressure in a single point, in this case at the middle of the sluice gate, oscillations are present but they

Figure 4.9 Pressure head: Experimental vs hydrostatic distribution

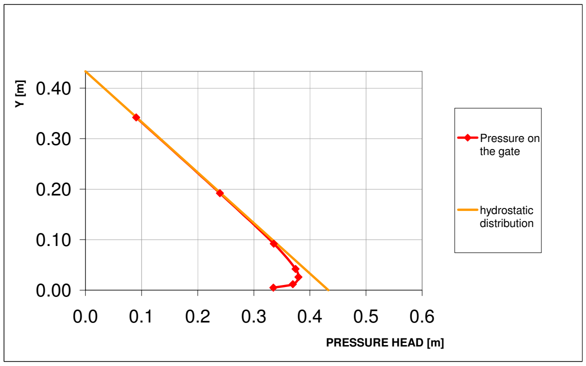

are acceptable if compared with the middle value (the horizontal line), in fact it is easy to calculate the standard deviation which is about an 11%.

4.6 The outing discharge

Keeping constant the upstream level, knowing the kind of sluice gate we are using and the entity of its uplift from the bottom of the channel, we have to know the precise value of the outing discharge of the under seal flow. Analyzing a single section of the outing flow we could risk to be influenced by a local alteration due for example to a wave, that is the reason why we integrate the data of velocity of each node of a vertical section along the height of the depth of water in that section and therefore we calculate the discharge; to give an example of the graph we have to integrate we can see fig. 4.13.

We consider five different vertical sections collocated, as we can see in tab.4.2, $5, 6, 7, 8, 10cm$ from the sluice gate respectively As we can see in tab.4.2 the error in the outing discharge is always lower that 10% if we exclude isolated phenomena, and if we remember the variation of the upstream discharge we can expect such results.

Table 4.2 Discharge of the under seal flow for different sections

t	Q_{theor}	$Q_{PFEM}[m^3/s]$				
$[s]$	$[m^3/s]$	x= 0.05	x= 0.06	x= 0.07	x= 0.08	x= 0.1
41.08	103.3	104.4	105	106	117.4	99.1
	Error	1%	2%	3%	14%	4.5%
47.76	103.3	104.6	92.8	102.6	106.5	104.6
	Error	1%	10%	1%	3%	1%
50	103.3	84.4	91.6	95.9	88.2	102.6
	Error	18%	11%	7%	15%	1%
63	103.3	106.4	111.5	111.	107.4	111.1
	Error	3%	8%	8%	4%	7%

Figure 4.10 Pressure head distribution: 1^{st} model

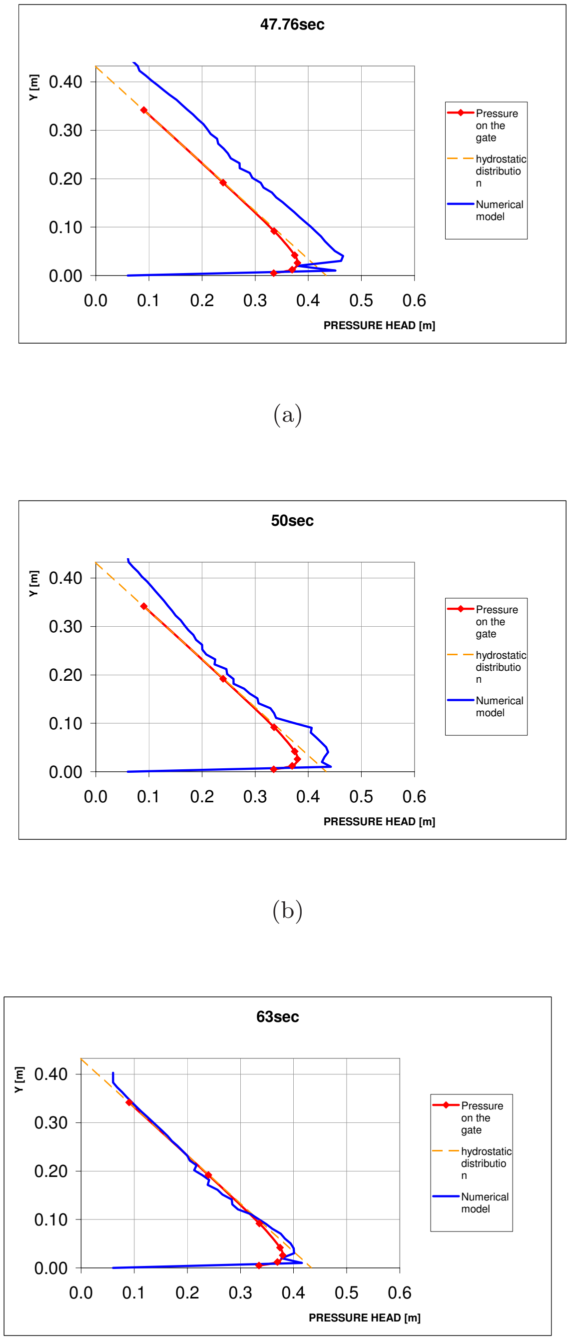

(a)

(b)

(c)

Figure 4.11 Pressure head distribution: 2^{nd} model

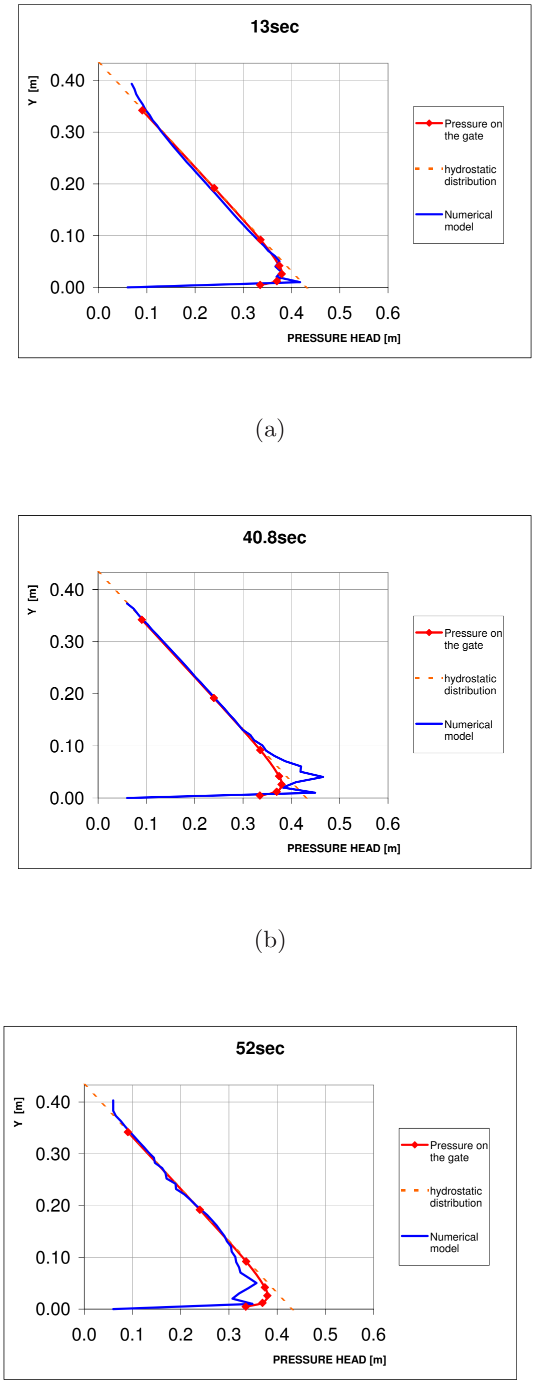

(a)

(b)

(c)

Figure 4.12 Pressure variation in time for the middle point of the sluice gate

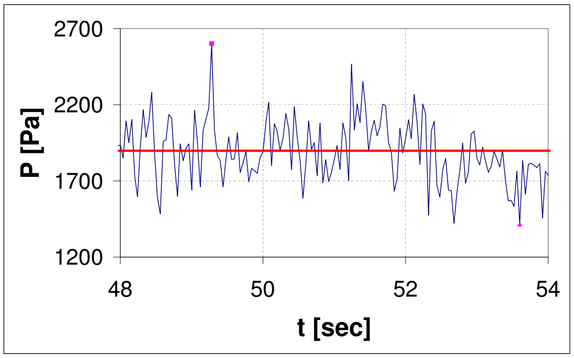

Figure 4.13 Velocity diagram for a vertical section 0.05cm far from the sluice gate

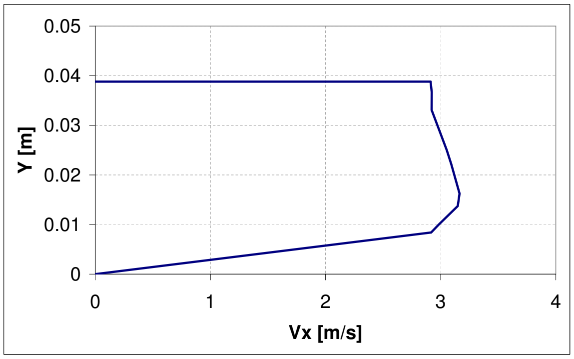

4.7 The analysis of the free surface of the downstream water

A thin and planar sluice gate as already said in 4.4 causes a contraction of the free surface of the flow bound to a contraction coefficient $C_c = 0.611$ following Kirchhoff method; that is, the under seal flow has to arrive having a depth of water which is equal to aC_c where a is the level of raisnes of the gate

It seems that the model cannot follow exactly the free surface of experimental results looking at fig.4.14 but we have to think that the mesh dimension is imposed equal to $0.008m$ at the beginning and, looking at the oscillation of the free surface, they are more or less of the same order, therefore it is impossible to appreciate a higher precision thinking in a discrete way.

Table 4.3 Depth of water between 10 and $50cm$ from the gate

t $[s]$	Medium depth $[m]$	Theoretical Value $[m]$	Standard Deviation
40.96	0.034	0.035	0.003
47.76	0.032	0.035	0.004
50	0.036	0.035	0.002

Looking at the values of the depth of water in the interval between $10cm$ and $50cm$ from the sluice gate and calculating a middle depth we obtain quite good results also comparing it with the standard deviation as we can see in tab. 4.3

Figure 4.14 Contraction after the sluice gate

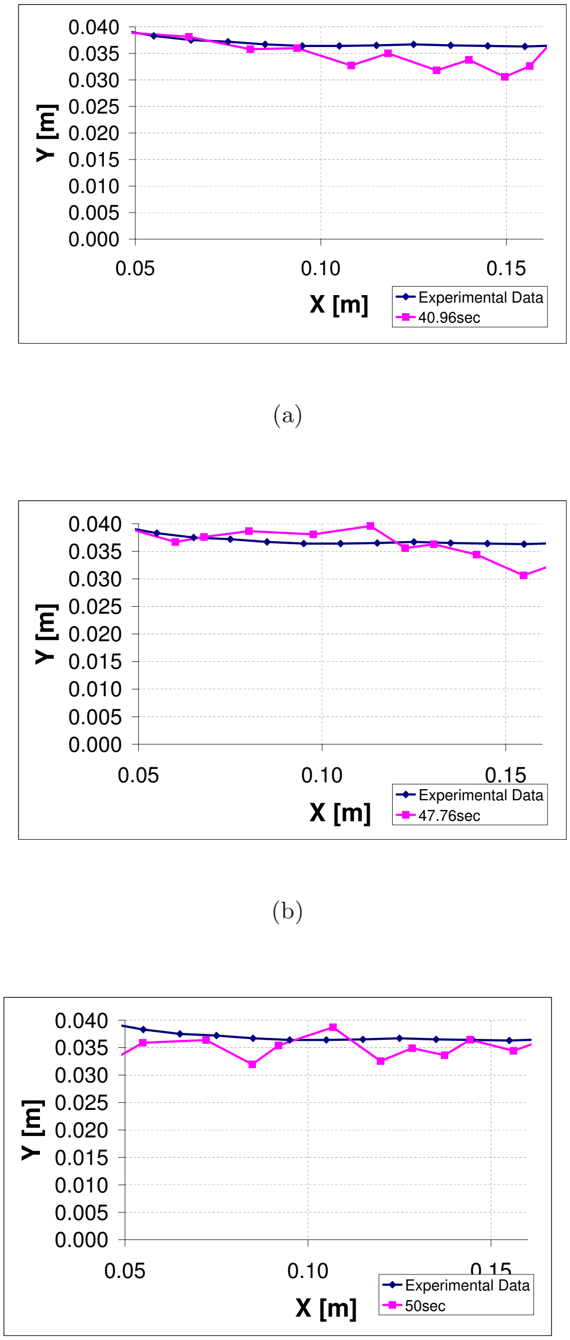

(a)

(b)

(c)

4.8 The hydraulic jump

One interesting phenomenon of energy dissipation generated by the clash of an upstream fast discharge with a downstream slow discharge is the hydraulic jump. Many forms of hydraulic jump exist and basically they are characterized by the *Froude Number* of the upstream discharge, in fact we have five different kinds of them:

- Wave hydraulic jump if $1 \leq Fr \leq 1.7$;
- Weak hydraulic jump if $1.7 \leq Fr \leq 2.5$;
- Oscillating hydraulic jump if $2.5 \leq Fr \leq 4.5$;
- Steady hydraulic jump if $4.5 \leq Fr \leq 9$;
- Strong hydraulic jump if $Fr \geq 9$;

Considering that for a generic section the total thrust is composed of two different parts:

- The hydrostatic thrust:

$$M_{hydr} = \gamma \cdot A \cdot y_G;$$

- The dynamic thrust:

$$M_{dyn} = \rho \cdot Q \cdot v;$$

Figure 4.15 Hydraulic jump, theoretical approach

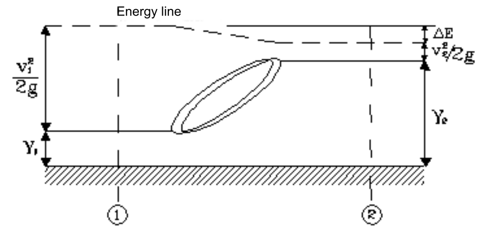

We know that an hydraulic jump is generated when the total thrust of the upstream discharge is equal to that of the downstream discharge; to localize it , once a control volume is defined, the momentum principle together with the continuity equation [12] [13] permit to obtain a relation between the upstream and the downstream motion; having a rectangular channel we can simplify the expression even more and we finally obtain:

$$\frac{y_2}{y_1} = \frac{-1 + \sqrt{1 + 8 \cdot Fr_1^2}}{2} \tag{4.3}$$

We can easily compare the development of the free surface in correspondence of the hydraulic jump having experimental data.

The kind of hydraulic jump we analyze is a steady one. Pink line represents experimental points whereas the blue and less regular one represents the model output. It is clear that the computational results are given for much more points than those which are taken into account in the experiment, being impossible to detect more than 10, 11 points.

Unfortunately for a phenomenon like an hydraulic jump, the output after few seconds is nothing really important, steady state and equilibrium between upstream and downstream channel are not fully obtained and only a qualitative behavior can be controlled.

Figure 4.16 Free surface development in hydraulyc jump

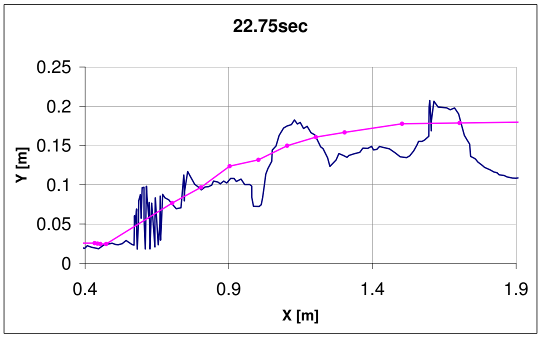

(a)

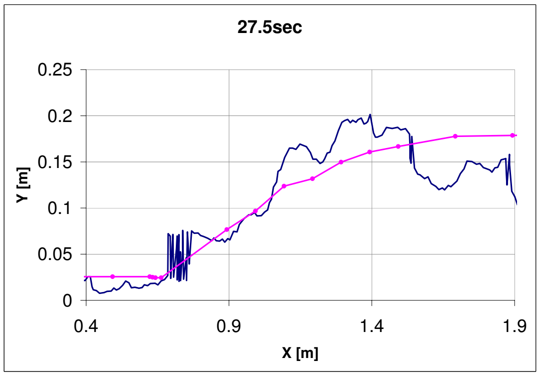

(b)

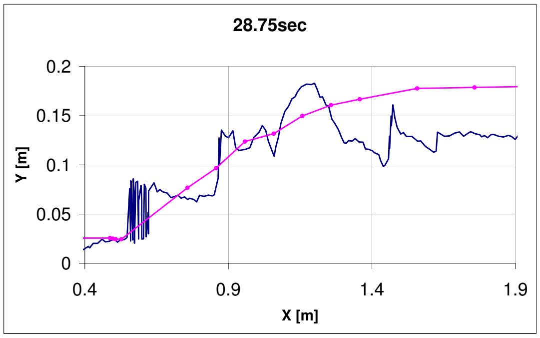

(c)

Chapter 5

Stepped Spillway

5.1 Abstract

The third example treated in this thesis is the experiment that analyzes the variables of the flux over a stepped spillway. After a brief description of what a stepped spillway is and of its principal utilizations, velocity and pressure on the steps of the crest will be analyzed. Air is not present in the highest part where the boundary turbulent layer is not still arrived at the free surface level.

5.2 Introduction

In the last years stepped spillways represent a choice more and more made to solve the problem of discharging water exceeding the maximum level allowed in a dam, on a downstream channel.

The origin of the construction of stepped spillway dates back to the ancient world if we think that the oldest still existing example is present in Arkanania (Greece) and it was built in the 1300 b.C. (5.1) [14]. It seems that the construction of this kind of structure was a common practice until the end of XIX century because, from one side, a good dam stability was ensured and from the other side it was possible to obtain a big energy dissipation; during XX century, on the contrary, it became more common the use of smaller (and therefore less expensive) structures with dissipation pools where the action of an hydraulic jump permits bigger dissipations. At the end of 70's the use of a new material such as roller-compacted concrete (RCC) gets

Figure 5.1 Arkanania Stepped spillway, Greece, 1300b.C.

Figure 5.2 Examples of stepped spillways in the past

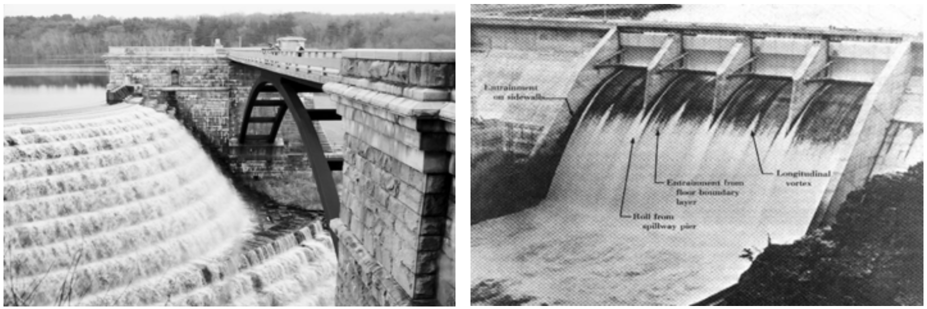

(a) Corton dam (1907) (b) Falvey (1980)

Figure 5.3 Examples of stepped spillways built with RCC

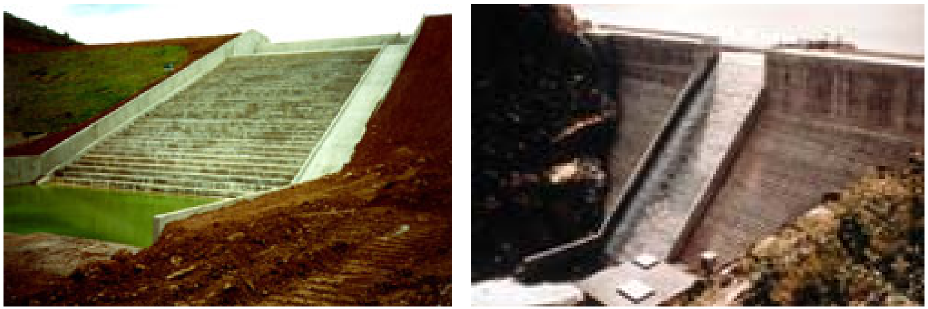

(a) (b)

raise the interest about stepped spillway.

Since 1980, RCC no-slump concrete has been used successfully to restore more than 100 dams and to build more than 70 new dams. RCC has three key properties that make it uniquely suited for dams: economy, performance, and high-speed construction. It has the strength and durability of conventional concrete that means much bigger than earth or rock-fill dam, but at a cost that rivals this other construction. RCC can be used to build new dams or to shore up old ones. It protects dams from over-topping failure, earthquakes, and erosion. This material has the same ingredients as conventional concrete: cement, water, and aggregates but it is much drier. It can be placed quickly and easily with large-volume earth-moving equipment. It's generally transported by dump trucks, spread by bulldozers, and compacted by vibratory rollers.

Sections are built lift-by-lift in successive horizontal layers so the downstream slope resembles a concrete staircase, an ideal technique for a stepped spillway that in fact are presents in the 30% of the RCC dams. Once a layer is placed, it can immediately support the earth-moving equipment to place the next layer. For existing earth and rock-fill dams, RCC acts like an armor plating to protect them from the erosion of high-velocity water flows. RCC can also be used to build new or replacement dams.

5.3 The experiment

The experiment we tried to reproduce was conducted by Prof.M.Sánchez-Juni and Dr.Eng.A. Táboas Amador en la Universitat Politecnica de Catalunya, at the Dip. de Ingenieria Hidraulica, Maritima y Ambiantal , UPC, E.T.S.

Figure 5.4 Experimental setting scheme

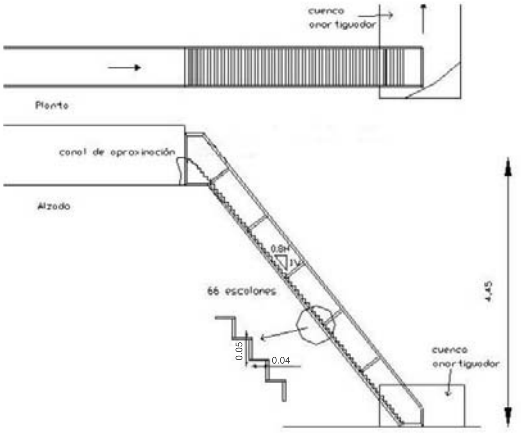

Figure 5.5 Variable steps

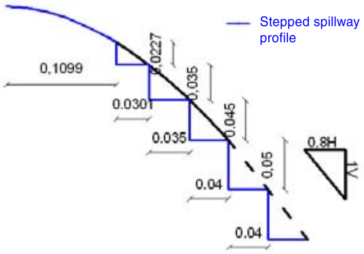

Ingenieros de Caminos, Canales y puertos de Barcelona, Spain. The analysis of the flux over stepped spillway was the subject of their Phd thesis [15] [16]. The reduced model used for the experiment is still present at the hydraulic and fluid mechanics laboratory at the UPC and it is a plexiglas horizontal upstream channel 5.8m long, and a plexiglas stairs that reproduces in the higher part the spillway profile following the equation

$$x^{1.85} = 2 \cdot 0.178^{0.85} \cdot y;$$

The height of the stair is 4.5m and the width, that coincides with that of the upstream channel, is 0.5cm. Excluding the first steps, represented in fig.5.5, the others have constant tread (0.04cm) and constant riser (0.05cm).

Figure 5.6 Experimental setting

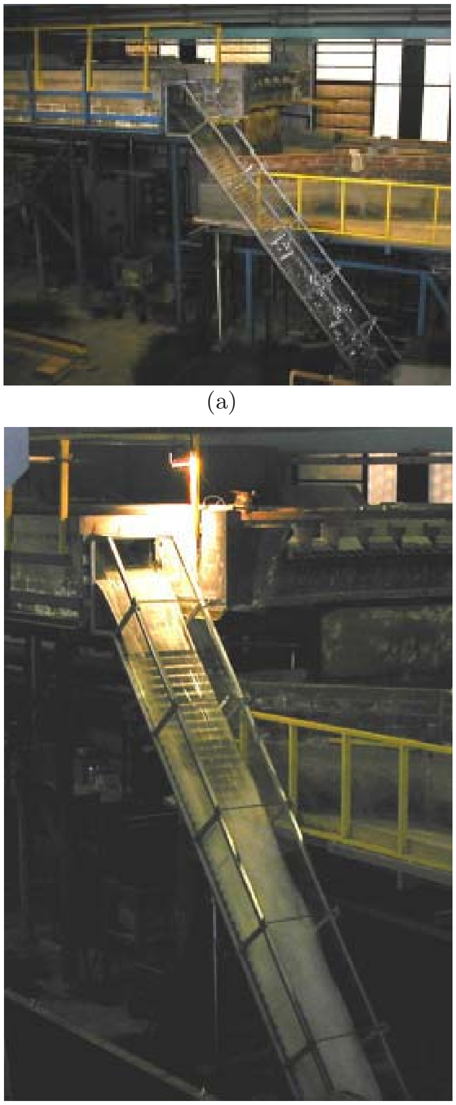

(a)

(b)

Figure 5.7 Analysis steps

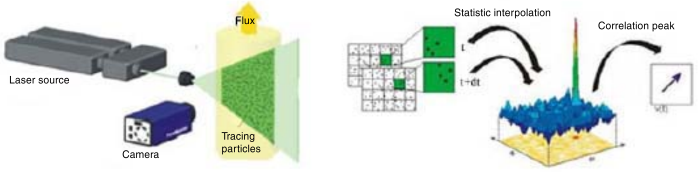

5.3.1 Velocities measurement techniques

For a given imposed upstream discharge, the aim of the experiment was to get quantitative values of the velocity field using an innovative technique: the *Particle Image Velocimetry (PIV)* which is, never the less than a optical method able to identify, for a given time instance all the velocity in a fixed plane. Velocity is deduced from the movements of the tracing particles which have to be able not to alter the fluid and also not to interact with it to be ideal particles. Looking at the position of the moving particle in two different time instance, measuring the position it is possible to deduce the velocity using statistic techniques. A laser was used as light source because of its ease to regulate and orientate and its wavelength is very short, of the order of about nanoseconds. A set of cameras was set to catch photos very close in time [16].

5.3.2 Pressure measurement techniques

For the dynamic pressure measurement piezoresistance sensors (see fig.5.9) have been used; these sensors were made of a silicon crystal in which an electric circuit was included. Pressure variation causes micro deformations in the crystal structure and these alterations are sufficient to change the electric circuit answer. A continuous excitation returns a signal which depends on the entity of pressure it has been subjected to [16] [15].

Figure 5.8 Laser input

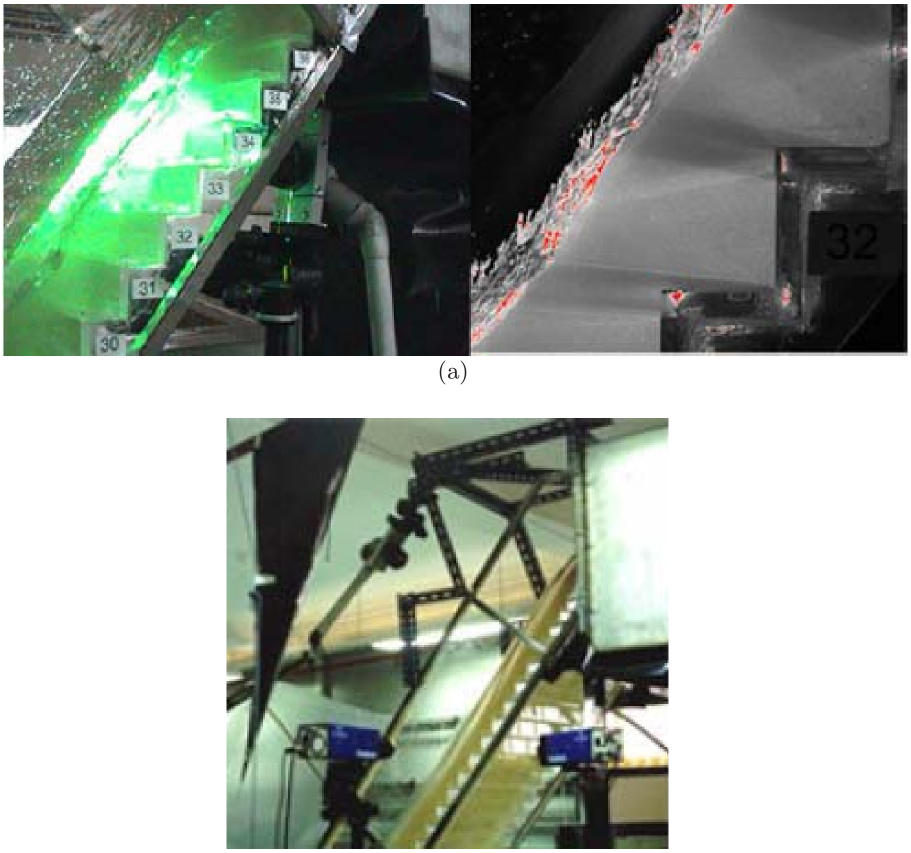

(a)

(b)

Figure 5.9 Pressure sensors

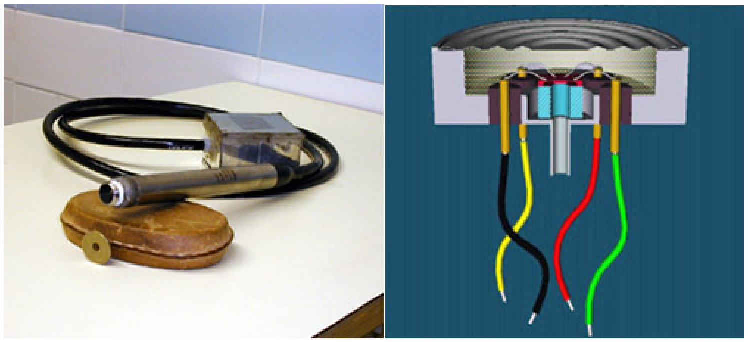

5.4 The model

A model was built to reproduce the phenomenon, the approach was a 2D one because it seems not necessary the third dimension also considering that all the experimental data have been surveyed in a plan $x - z$ where x is the direction of the flux and z is the vertical, and the collocation of the planes of analysis was as far from the lateral wall as it was sufficient not to feel the edge effects.

Geometry was very simple to build and boundary conditions were imposed knowing the discharge value and the upstream water depth. A fluid-in line (already described in cap 3, par 3.5) was built $1.5m$ upstream from the beginning of the spillway crest, from that line the flux of uniform slow motion begins, once the flow starts to go down on the spillway, the motion became a fast one, the depth of water reduces and velocity increases as it is easy to imagine.

Experimental data inserted in the model are the following:

- The *discharge* is $55l/s$ and because the channel width is $0.5m$ the specific discharge is $0.11m^3/sm$;

- The inflow depth is $0.178m$ over the spillway crest;

As it is easy to verify the initial discharge is a slow flux. At the beginning this represented a problem in the creation of fluid particles: it seemed that once a set of node was created, the following set does not have the force to push the first set forward, it seemed that a node found a wall in front of itself becoming impossible the creation of other fluid, the only possibility for the just created nodes was velocity vector turned in the opposite verse causing an outing of water in the wrong direction if compared with what was expected.

This was a consequence of the difficulties to impose initial conditions: velocity is usually given as a constant value on the all fluid-in line, the real velocity distribution (with $v = 0m/s$ on the interface fluid-structure and v_{max} on the free surface) will be created automatically at the following time steps with the boundary conditions; a more difficult problem can arise with pressure, some people impose the hydrostatic distribution, some other do not impose any pressure, both techniques are incorrect, but they leave

Figure 5.10 Distorsion of velocity verse

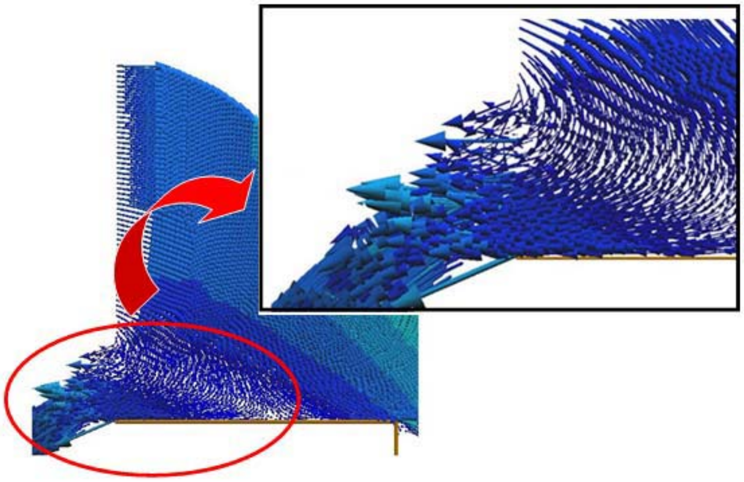

the definition of a pressure distribution at the already created particles as happen for the velocity.

The *PFLOW program* initially had this second approach, the solution of this problem has been found out considering the fluid-in line and only this line (not the created particles) as solid, it is like to say that there is a wall from what fluid is generated, and it automatically induces a real pressure distribution to the detaching nodes of the fluid (for more details on the difference between fluid-in and solid: cap 3, par 3.5).

The model does not represent the entire stair, but finishes after the

Figure 5.11 Th 2D model

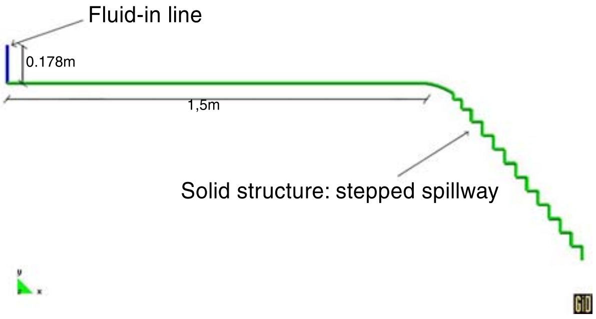

Figure 5.12 Flux on a stepped spillway

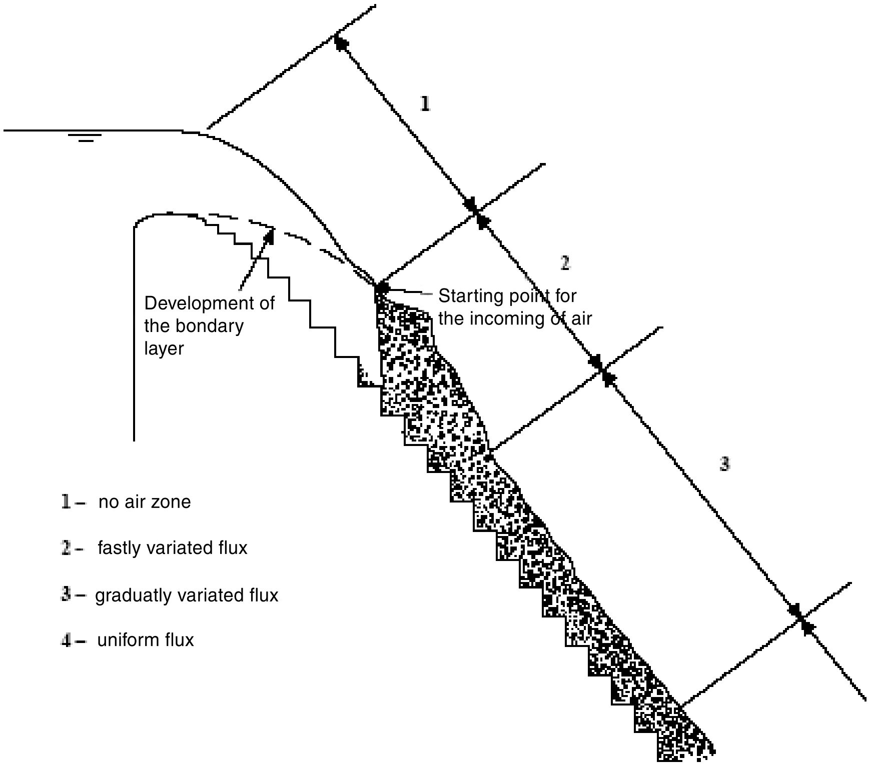

Figure 5.13 Line that separate the no aired zone from the turbulent zone

Figure 5.14 Velocity field next to step 34 and 35

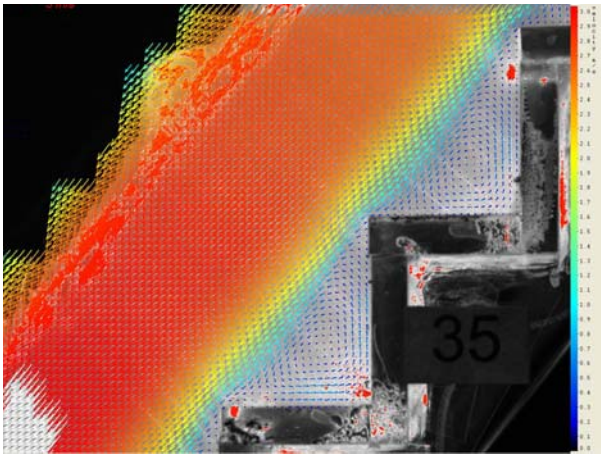

first thirteen step. In fact the object of the analysis is the upper part of the spillway, that is, the non aired flux (fig. 5.12): after these first steps air starts to get inside the flux because of the arriving of the turbulent boundary layer to the free surface [12], creating a fluid that is not water any more, but it is a mixture between air and water; this different behavior is clear in the photo 5.13.

The turbulent boundary layer thickness (δ) grows progressively until it arrives at the value of the flow depth; after that moment turbulent fluctuations are sufficient to overcome the viscosity force and the superficial tension creating perturbations that allow the entry of the air. We concentrates on the part where there is no air.

Being the flow over the spillway a fast discharge with *Froude Number*> 1 the downstream conditions do not influence the upstream discharge, it is sufficient to end the solid structure, creating a free flow.

For the analysis of pressure and velocity each step has been numerated starting from step number 40 at the crest of the stepped spillway and going down.

5.4.1 Velocity

Vectorial field photographed in fig. 5.14 clearly shows the development of two completely different flows over the stepped spillway:

- A superior discharge that flows over the steps with a velocity which is ten times higher then that developed in the steps;

- A recirculatory discharge that develops in the cavity delimited by the risers of the steps.

In the small transitory zone between these two fluxes a very big velocity gradient is present, it is the zone of exchange of momentum.

Velocity is well reproduced from the model with an high precision, see for instance fig. 5.15, fig. 5.15, fig. 5.16, fig. 5.17 where isotaches are traced with different colors. We expected that the first isotach not influenced by the presence of the stairs is the one with $v = 2m/s$ and looking at the green line it is exactly like this; velocity in the cavity of each step is recirculatory and ten time smaller than the superior discharge.

Figure 5.15 Steps 31 and 32 after 3.4sec

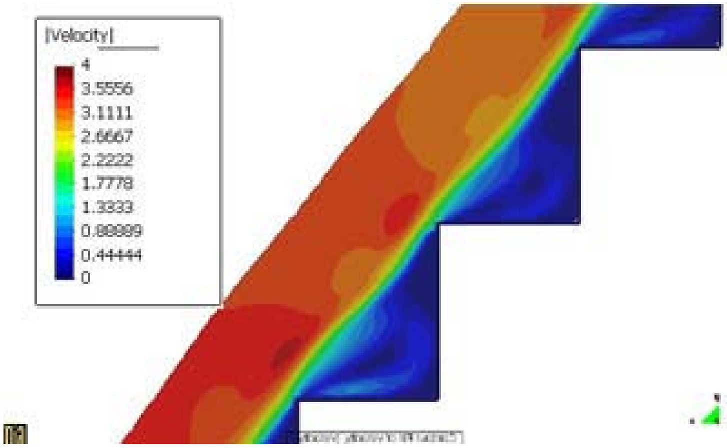

(a) Computational results

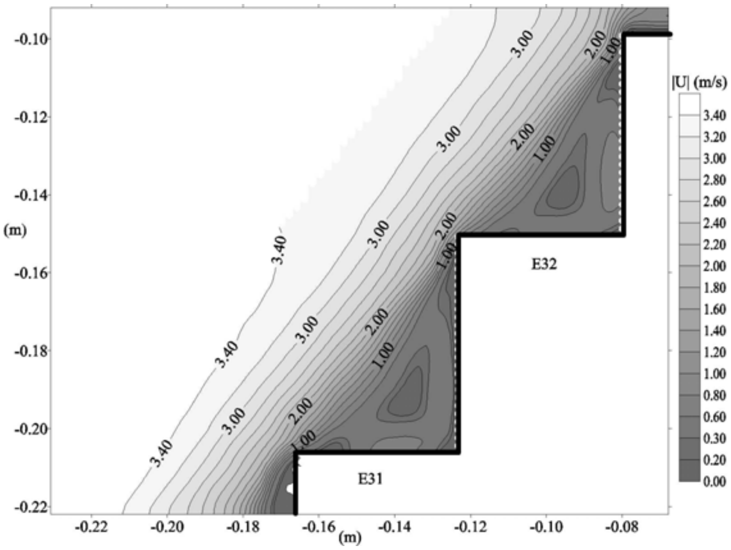

(b) Experimental results

Figure 5.16 Steps 34 and 35 after 3.4sec

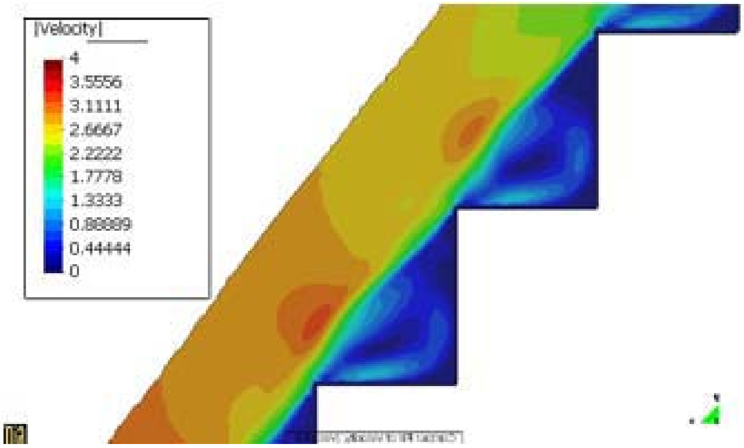

(a) Computational results

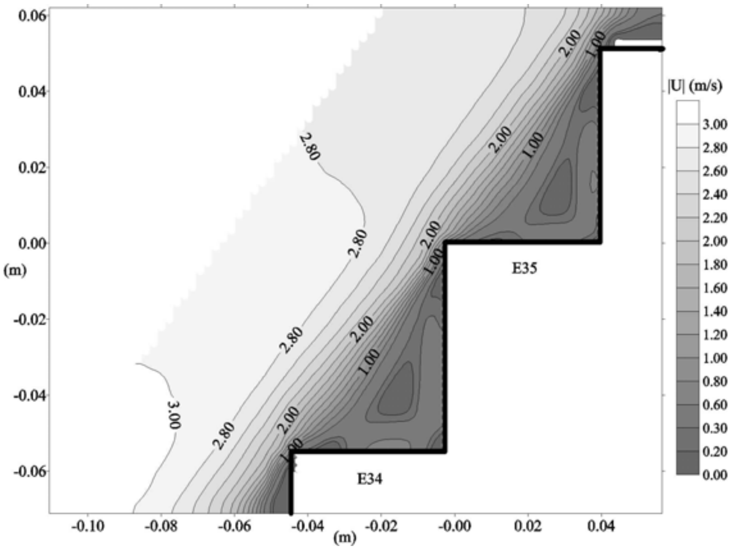

(b) Experimental results

Figure 5.17 Steps 31 and 32 after 3.7sec

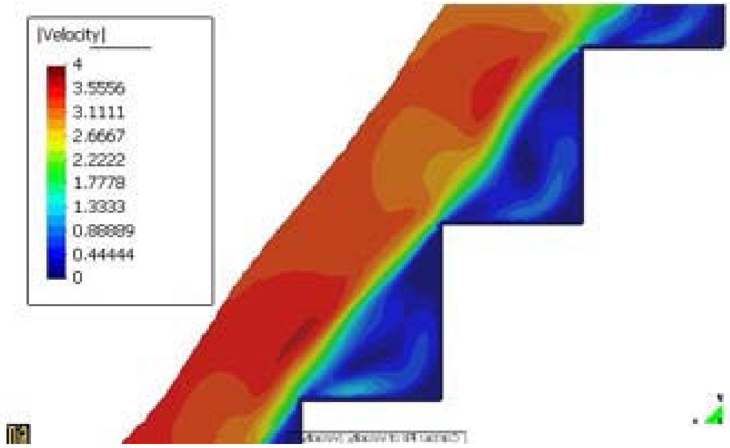

(a) Computational results

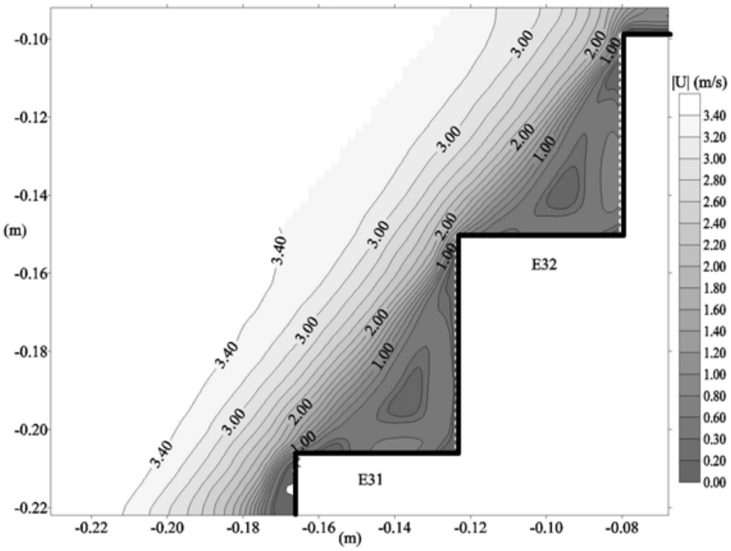

(b) Experimental results

Figure 5.18 Steps 34 and 35 after 3.7sec

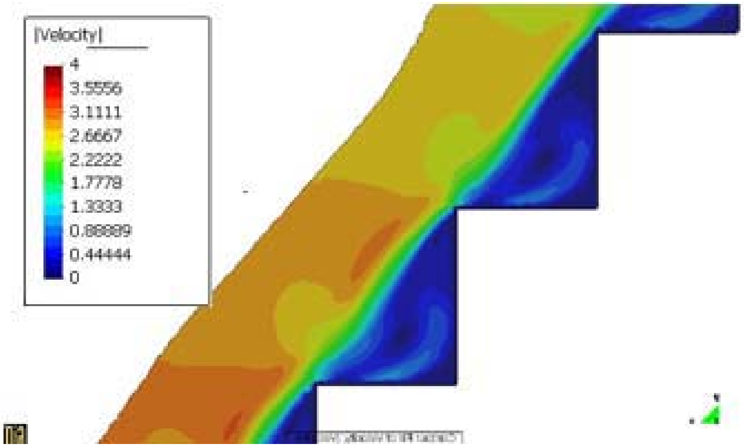

(a) Computational results

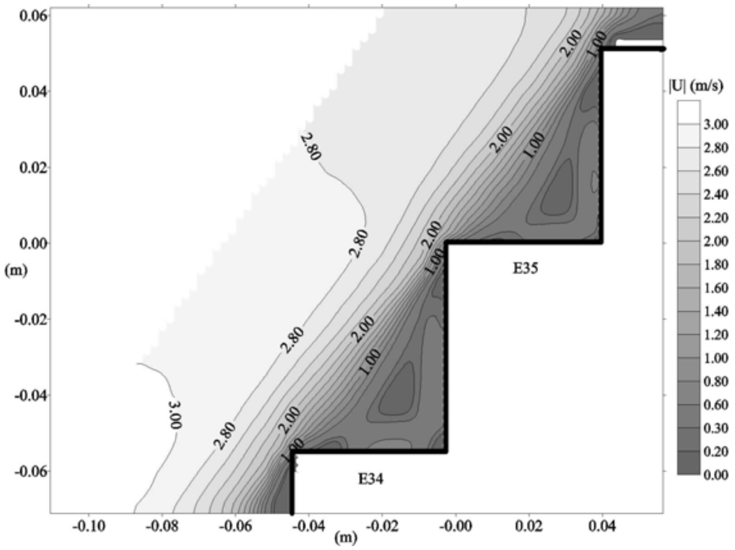

(b) Experimental results

5.4.2 Pressure

The analysis of pressure distribution on the steps would need a long period of observation to achieve to the same results present in the Phd thesis of Dr. Amador [16]. He calculate a mean pressure on the fixed measure points of each step considering time intervals ($\tilde{2}0min$) much longer than the few seconds of our computational results.

A low precision in the comparison is the direct consequence of such a difference, this means that only a qualitative behavior can be controlled.

Some problems are clearly shown in the graphs of the risers much than in that of the treads where the behavior is much more similar. Mean pressure value are always negative in the upper part of the riser of the computational model, while they have a value which is next to zero in the experimental data. That is a zone where there is the separation between the superior flux and the vortex in the step cavity. The biggest fluctuations of pressure value are present in that zone, as proved experimentally.

The following graphs analyze pressure value in function of the position on the tread or on the riser, treating the different quantities in an a-dimensional way: mean pressure head value is calculated for each of the five points of the riser and the seven of the tread. p/γ is divided respectively by the length of the tread or of the riser. The points of the analysis where indicated in an adimensional way too, dividing the abscissa or the ordinate by the length of the riser or of the tread too.

Figure 5.19 Velocity field next to step 34 and 35

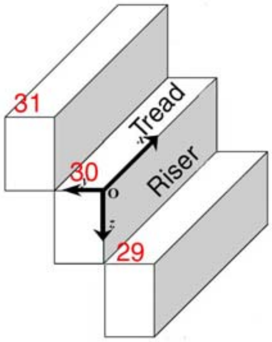

Figure 5.20 Step 29: experimental data (green line with triangles) and computational output (blue line with squares)

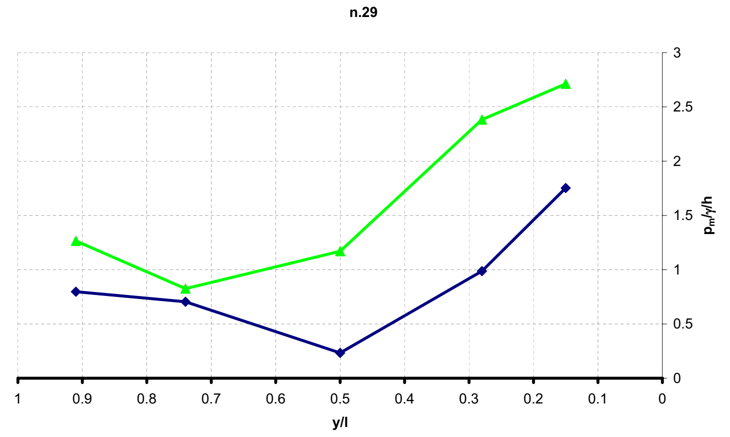

(a) Tread

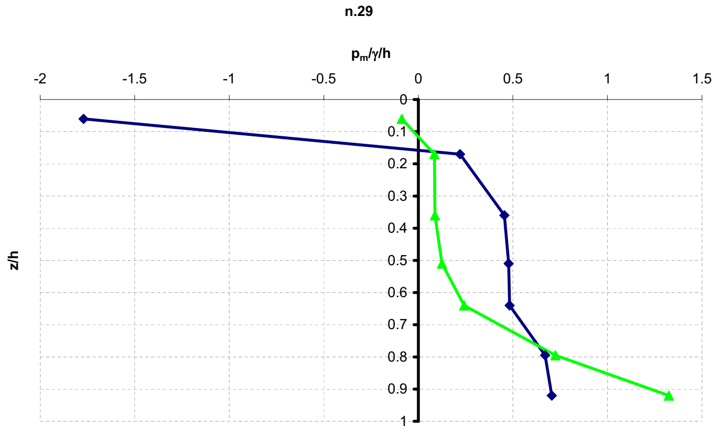

(b) Riser

Figure 5.21 Step 30: experimental data (green line with triangles) and computational output (blue line with squares)

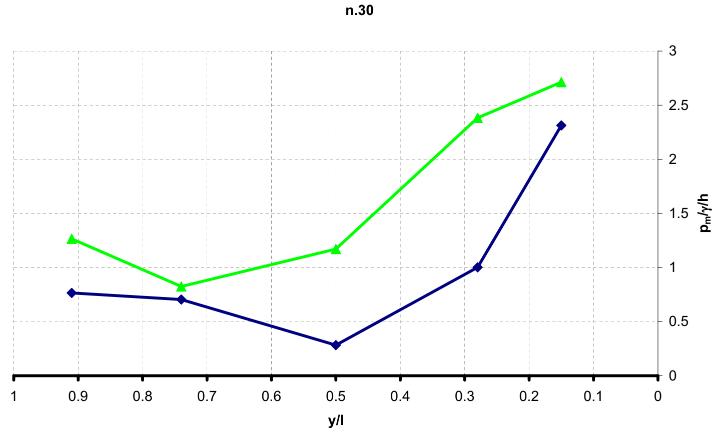

(a) Tread

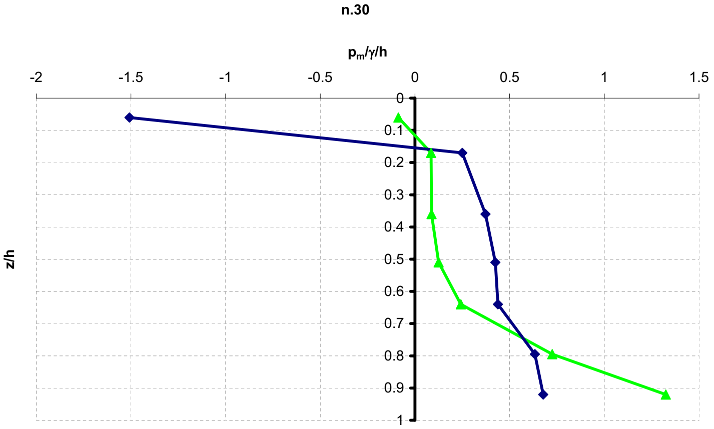

(b) Riser

Figure 5.22 Step 31: experimental data (green line with triangles) and computational output (blue line with squares)

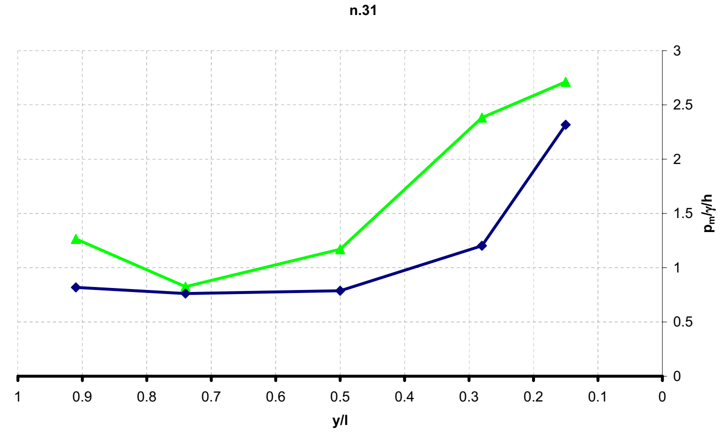

(a) Tread

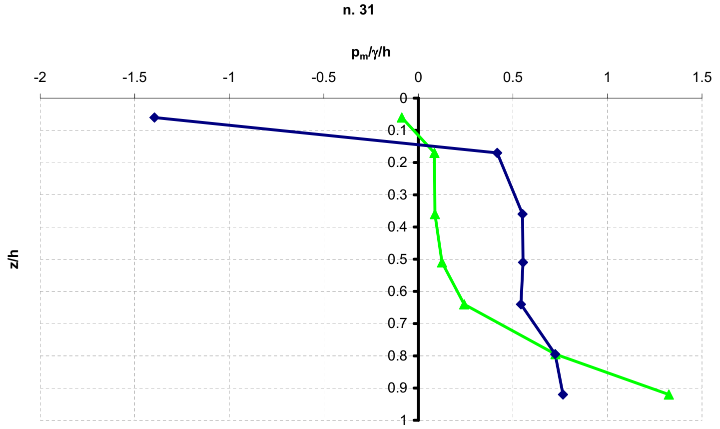

(b) Riser

Appendix A

Descriptions of motion

A.1 Introduction

A very important aspect, during the development of a computer code, is the choice of an appropriate *kinematical description* of the continuum. In fact all the relationship between the deforming continuum and the grid of the computational mesh are determined by this choice and overall in fluid mechanics problems, one of the big difficulty is the ability to catch and follow the big distortions and changes at the interface between two different fluids or fluid and structure.

In literature two classical descriptions of motion are present: the *Lagrangian* and the *Eulerian* descriptions, both approaches have advantages and drawbacks that are going to be outlined in this section; there is a third description that will be presented and that tries to combine all the advantages of both the classical kinematical description while minimizing their respective drawbacks as far as possible.

Lagrangian algorithms are mainly used in structural mechanics having each individual node of the computational mesh that follows the associated material particle during motion. This is a good way to trace easily the interface fluid-fluid or fluid-structure and to consider materials with history-dependent constitutive relations. Its weakness is the inability to follow big distortions of the domain without the necessity of a continuum remeshing.

Eulerian algorithm on the contrary, is largely used in fluid dynamics because of the ease to follow also large movements: in fact in this case the computational mesh is fixed and the continuum moves in respect to the grid,

Figure A.1 1D example of the three different kinematical representations

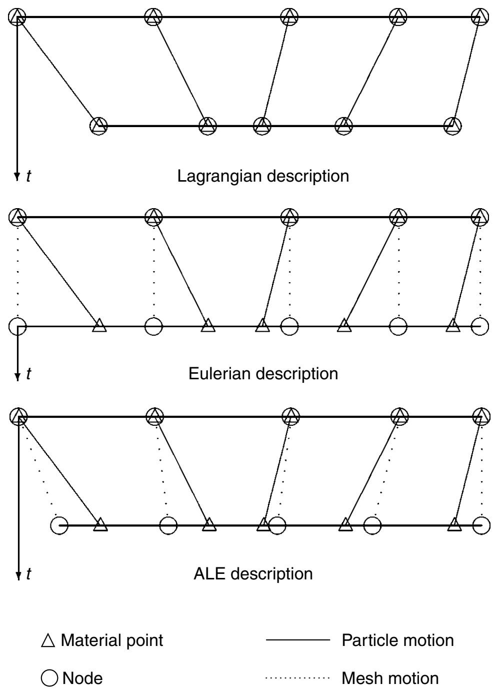

it is more difficult, in this case, to be able to follow the interfaces with big detail.

A third technique has been developed to combine the best feature of both Lagrangian and Eulerian approach, it is known as *arbitrary Lagrangian-Eulerian (ALE) description*. In this case the nodes of the computational mesh may move with the continuum (as in Lagrangian representation) or may be fixed (as in Eulerian one) or may move in some arbitrarily way to permit a continuous rezoning capability. Doing this its easier to catch big distortions than with Lagrangian method and the resolution is better than that afforded by purely Eulerian approach [17],[3].

A.2 Lagrangian and Eulerian viewpoints

Material domain $\mathbf{R}_{\mathbf{X}} \subset \mathbb{R}^{n_{sd}}$, with n_{sd} spatial dimension, and spatial domain $\mathbf{R}_{\mathbf{x}}$ are the two traditional domains used in continuum mechanics: the first one is consisting of material particles $\mathbf{X}$, the second one of spatial points

Figure A.2 Lagrangian description of motion

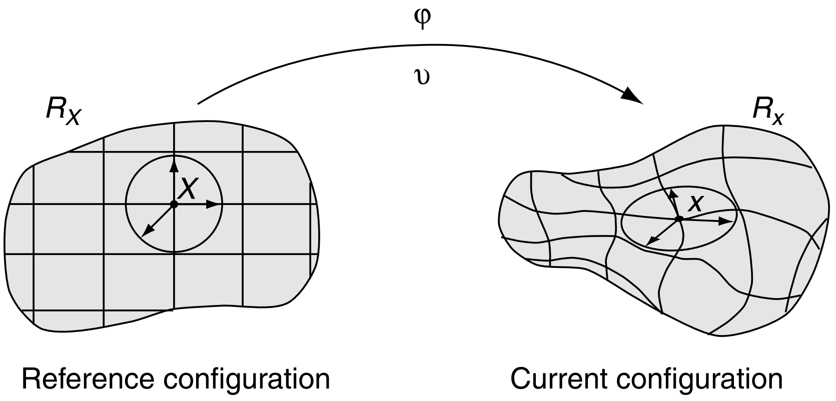

$\mathbf{x}$. As outlined in A.1, the Lagrangian approach consists in following the material particles in their motion, that is, once a computational grid is introduced to follow the continuum particle motion, then , the two entities will be permanently connected. The motion of the material points relates the material coordinates $\mathbf{X}$, to the spatial one $\mathbf{x}$ and it is defined by a function φ

$$\varphi : \mathbf{R_X} \times [t_0, t_{final}\,[\longrightarrow \mathbf{R_x} \times [t_0, t_{final}\,[$$

$$(\mathbf{X}, t) \longrightarrow \varphi\,(\mathbf{X}, t) = (\mathbf{x}, t) \tag{A.1}$$

That means that $\mathbf{X}$ and $\mathbf{x}$ can be linked in time by the low of motion:

$$\mathbf{x} = \mathbf{x}(\mathbf{X}, t) \qquad t = t \tag{A.2}$$

From that statement it can be deduced that: the spatial coordinates $\mathbf{x}$ depend both on the material particle $\mathbf{X}$, and time t, and physical time is measured by the same variable t in both domains. Using a matrix representation

$$\frac{\partial \varphi}{\partial(\mathbf{X}, t)} = \begin{pmatrix} \frac{\partial \mathbf{x}}{\partial \mathbf{X}} & \mathbf{v} \\ \mathbf{0}^T & 1 \end{pmatrix}; \tag{A.3}$$

where $\mathbf{0}^T$ is a null vector and

$$\mathbf{v}(\mathbf{X}, t) = \left.\frac{\partial \mathbf{x}}{\partial t}\right|_x \tag{A.4}$$

The one-to-one mapping φ must verify

$$det(\frac{\partial \mathbf{x}}{\partial \mathbf{X}}) \geq 0 \qquad \forall \mathbf{X}, \forall t \geq t_0$$

Because the material points coincide with the same grid points during the whole motion, there are no convective terms in Lagrangian formulation: the material derivative reduces to a simple time derivative. This last aspect is one of the bigger advantages in computational calculation, but especially in fluid dynamics problems, Lagrangian algorithms undergo a loss of accuracy and can also be unable to finish a calculation because of the excessive distortions of the computational mesh.

This particular problem is overcame by the Eulerian formulation which keeps fixed the computational mesh allowing the material particles to move freely: it examines the physical quantities associated with the fluid particles passing through a fixed region of space. The material velocity corresponds to the velocity of the material points coincident with the considered node at a given time t. In this case there is no reference to the initial configuration an the material coordinate $\mathbf{X}$ as happened in Lagrangian description

$$\mathbf{v} = \mathbf{v}(\mathbf{x}, t). \tag{A.5}$$

The biggest problem from a computational point of view is the appearance of a convective term being mesh nodes dissociated from continuum particles and serious difficulties are now found in following deforming material interfaces and mobile boundaries.

A.3 ALE description of motion

Arbitrary Lagrangian-Eulerian (ALE) methods were first presented in finite difference and finite volume context and then developed since late 60's by Noa(1964), Frank and Lazarus (1964), Trulio (1978), Hirt (1974) [17]. The so called referential configuration $\mathbf{R}_\chi$, a third domain, different from both the spatial and the material domain, is introduced; in that case reference

Figure A.3 ALE description of motion

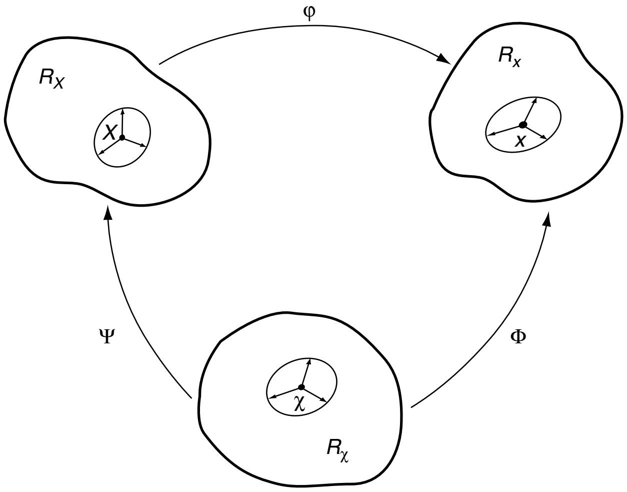

coordinates χ are introduced to identify the grid points as in fig.A.3. $\mathbf{R}_\chi$ is mapped into the material and spatial domains by $\boldsymbol{\Psi}$ and $\boldsymbol{\Phi}$ respectively; we can write $\varphi = \boldsymbol{\Phi} \circ \boldsymbol{\Psi}^{\mathbf{-1}}$ to underline that the three domains cannot be independent.

Form the referential to the spatial domain the motion of the grid points can be described with

$$\boldsymbol{\Phi} : \mathbf{R}_\chi \times [t_0, t_{final} [\longrightarrow \mathbf{R}_{\mathbf{x}} \times [t_0, t_{final} [$$

$$(\chi, t) \longrightarrow \boldsymbol{\Phi} (\chi, t) = (\mathbf{x}, t) \tag{A.6}$$

with this gradient

$$\frac{\partial \boldsymbol{\Phi}}{\partial (\chi, t)} = \begin{pmatrix} \frac{\partial \mathbf{x}}{\partial \chi} & \mathbf{v} \\ \mathbf{0}^T & 1 \end{pmatrix}; \tag{A.7}$$

the mesh velocity is

$$\hat{\mathbf{v}}(\chi, t) = \left. \frac{\partial \mathbf{x}}{\partial t} \right|_\chi \tag{A.8}$$

From referential to material domain on the contrary

$$\boldsymbol{\Psi}^{-1} : \mathbf{R}_{\mathbf{X}} \times [t_0, t_{final}\,[\; \longrightarrow \mathbf{R}_{\chi} \times [t_0, t_{final}\,[$$

$$(\mathbf{X}, t) \longrightarrow \boldsymbol{\Psi}^{-1}(\mathbf{X}, t) = (\chi, t) \tag{A.9}$$

and its gradient is

$$\frac{\partial \boldsymbol{\Psi}^{\mathbf{-1}}}{\partial(\mathbf{X}, t)} = \begin{pmatrix} \frac{\partial \chi}{\partial \mathbf{X}} & \mathbf{w} \\ \mathbf{0}^T & 1 \end{pmatrix}; \tag{A.10}$$

where the velocity, that can be read as the particle velocity in the referential domain, is defined as

$$\mathbf{w} = \left.\frac{\partial \chi}{\partial t}\right|_{\mathbf{X}} \tag{A.11}$$

The relation between the three different velocities can be obtained differentiating the expression $\varphi = \boldsymbol{\Phi} \circ \boldsymbol{\Psi}^{\mathbf{-1}}$,that is, in matrix term,

$$\begin{pmatrix} \frac{\partial \mathbf{x}}{\partial \mathbf{X}} & \mathbf{v} \\ \mathbf{0}^{\mathbf{T}} & 1 \end{pmatrix} = \begin{pmatrix} \frac{\partial \mathbf{x}}{\partial \chi} & \hat{\mathbf{v}} \\ \mathbf{0}^{\mathbf{T}} & 1 \end{pmatrix} \cdot \begin{pmatrix} \frac{\partial \chi}{\partial \mathbf{X}} & \mathbf{w} \\ \mathbf{0}^{\mathbf{T}} & 1 \end{pmatrix} \tag{A.12}$$

From that system we can obtain

$$\mathbf{v} = \hat{\mathbf{v}} + \frac{\partial \mathbf{x}}{\partial \chi} \cdot \mathbf{w} \tag{A.13}$$

and wanting to put in evidence the value of the convective term (the relative velocity between the material and the mesh), we obtain

$$\mathbf{c} := \mathbf{v} - \hat{\mathbf{v}} = \frac{\partial \mathbf{x}}{\partial \chi} \cdot \mathbf{w} \tag{A.14}$$

We have to be careful not to confuse the particle velocity $\mathbf{w}$ that is seen from the referential domain, with the convective one $\mathbf{c}$, which is the particle velocity relative to the mesh, seen from the spatial domain $\mathbf{R}_{\mathbf{X}}$

As it is easy to see from ALE equation both Lagrangian and Eulerian formulation can be obtained, respectively taking $\boldsymbol{\Psi} = \mathbf{I}$ we obtain $\mathbf{X} \equiv \chi$ and the convective velocity is null, or taking $\boldsymbol{\Phi} = \mathbf{I}$ we obtain $\mathbf{x} \equiv \chi$ and the material velocity $\mathbf{v}$ is equal to the convective $\mathbf{c}$.

Bibliography

[1] *GiD, The personal pre and post processor.* http://gid.cimne.upc.es.

[2] C.A.Felippa. *Introduction to Finite Element Methods.* 2005.

[3] A. Huerta J.Donea. *Finite Elements Methods for Flow Problems.* Wiley, 2003.

[4] R.L.Taylor O.C.Zienkiewicz. *Vol. 3. The finite element method. Fluid dynamics.* Butterworth Heinemann, 2000.

[5] J. Morfett A.Chadwick. *Hydraulics in Civil and Environmental Engineering.* E-FN Spon, 1998.

[6] Riccardo Rossi. *Light weight Structures: structural analysis and coupling issues.* PhD thesis, Universita di Bologna, 2004.

[7] E.Oñate R.Idelsohn. To mesh or not to mesh.this is the question... *Computer Methods in Applied Mechanics and Engineering*, 2006.

[8] N. Calvo F.Del Pin R.Idelsohn, E.Oñate. The meshless finite element method. *International Journal for Numerical Methods in Engineering*, 58:893–912, 2003.

[9] E.P.Mucke H. Edelsbruner. Three dimensional alpha.shape. *ACM Transaction on Graphics*, 13:43–72, 1994.

[10] W.H. Hager R.Juon. Flip bucket without and with deflec. *Journal of Hydraulic Engineering*, 126:837–845, 2000.

[11] W. H. Hager V. Heller. Ski jump hydraulics. *Journal of Hydraulic Engineering*, 131:347–355, 2005.

[12] A.Ghetti. *Idraulica*. Cortina, 1984.

[13] R.Cola. *Idraulica*. IMAGE, 2002.

[14] H.Chanson. *The hydraulics of stepped chutes and spillways*. Balkema, Rotterdam, 2002.

[15] M.Sánchez-Juni. *Comportaminento hidraulico de los haliviadero escalonados en presa de hormigon compactado. Analis del campo de presiones*. PhD thesis, 2001.

[16] A.Táboas Amador. *Comportaminento hidraulico de los haliviadero escalonados en presa de hormigon compactado*. PhD thesis, 2004.

[17] J.Ph. Ponthot A. Rodríguez-Ferran J.Donea, A. Huerta. *Encyclopedia of Computational Mechanics, Volume 1, chapter 14, Arbitrary Lagrangian-Eulerian Methods*. John Wiley and Sons, 2004.